AGU PUBLICATIONS

JGR

Journal of Geophysical Research: Oceans

RESEARCH ARTICLE

10.1002/2015JC011160

Turbulent plumes from a glacier terminus melting in a stratified ocean

Samuel J. Magorrian[1] and Andrew J. Wells[1]

[1]Atmospheric, Oceanic, & Planetary Physics, Department of Physics, University of Oxford, Oxford, UK

Key Points:
- We model ice shelf and glacier terminus melting controlled by meltwater convection in the ocean
- We find scaling laws for ice melt in a linearly stratified ocean for use in parameterizations
- We determine the sensitivity of melt to ocean temperature and salinity, and ice shelf basal slope

Supporting Information:
- Supporting Information S1

Correspondence to:
A. J. Wells,
andrew.wells@physics.ox.ac.uk

Citation:
Magorrian, S. J., and A. J. Wells (2016), Turbulent plumes from a glacier terminus melting in a stratified ocean, *J. Geophys. Res. Oceans*, *121*, 4670–4696, doi:10.1002/2015JC011160.

Received 21 JUL 2015
Accepted 1 JUN 2016
Accepted article online 6 JUN 2016
Published online 10 JUL 2016

Abstract The melting of submerged faces of marine-terminating glaciers is a key contributor to the glacial mass budget via direct thermodynamic ablation and the impact of ablation on calving. This study considers the behavior of turbulent plumes of buoyant meltwater in a stratified ocean, generated by melting of either near-vertical calving faces or sloping ice shelves. We build insight by applying a turbulent plume model to describe melting of a locally planar region of ice face in a linearly stratified ocean, in a regime where subglacial discharge is insignificant. The plumes rise until becoming neutrally buoyant, before intruding into the ocean background. For strong stratifications, we obtain leading-order scaling laws for the flow including the height reached by the plume before intrusion, and the melt rate, expressed in terms of the background ocean temperature and salinity stratifications. These scaling laws provide a new perspective for parameterizing glacial melting in response to a piecewise-linear discretization of the ocean stratification.

1. Introduction

The ablation of marine-terminating ice sheets into the ocean is of interest for projections of ice sheet dynamics and sea level rise [*IPCC*, 2013; *Straneo et al*., 2013], and for predictions of freshwater fluxes to the polar oceans with consequent impacts on climate [e.g., *Gade*, 1979; *Foldvik and Gammelsrød*, 1988; *Vellinga and Wood*, 2002; *Jacobs et al*., 2011; *Bintanja et al*., 2013]. Recent observations in Greenland and Antarctica show enhanced ice sheet discharge coincident with ocean warming [e.g., see *Holland et al*., 2008a; *Pritchard et al*., 2012; *Rignot et al*., 2013; *Straneo and Cenedese*, 2015] for marine ice sheets running into the ocean via either floating ice shelves or near-vertical calving faces. Ocean warming can force mass loss directly, via thermodynamic ablation of ice, or indirectly if melting leads to undercutting and enhanced calving of icebergs [*O'Leary and Christoffersen*, 2013].

The thermodynamic ablation of a near-vertical glacier terminus or the sloping base of an ice shelf is primarily controlled by the rate of heat and salt supply from the ocean to the ice [cf., *Sergienko et al*., 2013]. Thermodynamic ablation can correspond to either melting of ice controlled primarily by the supply of heat to the ice-ocean interface, or dissolution of the ice in a cooler ocean when the rate of salt transfer controls the ablation rate via its impact on the salinity-dependent freezing temperature [e.g., *Woods*, 1992; *Wells and Worster*, 2011; *Kerr and McConnochie*, 2015]. For notational brevity, we will use the term melting to refer to thermodynamic ablation in a general sense throughout the remainder of this paper, noting that this encompasses both cases of melting and dissolution without distinction. Ocean heat and salt transfer are modulated by a range of dynamical processes that are relevant in different settings, including tidal flows [e.g., *Holland*, 2008; *Mueller et al*., 2012], nearly geostrophic ocean currents [e.g., *Holland et al*., 2008b; *Little et al*., 2009], ocean waves [*Josberger*, 1978], and buoyancy-driven meltwater flows [e.g., *Jenkins*, 1991; *Payne et al*., 2007; *Jenkins*, 2011]. We focus on buoyancy-driven flows here. When ice melts into the ocean, the meltwater is fresher than the ambient seawater, providing a source of buoyancy that drives convective flow along the ice face in a turbulent plume. Flow in the turbulent plume is greatly enhanced when there is a substantial subglacial discharge [*Jenkins*, 2011]. However, such subglacial discharge is not necessary for the development of flow, which can also develop due to direct melting of the ice face (e.g., see *Jenkins* [1991] in a numerical context, or *Wells and Worster* [2008] and *Wells* [2008] for an analytical treatment of dynamically similar flows). The turbulent motion entrains the neighboring warm seawater into the plume, which further enhances melting. Thus, when external mechanically driven sources of turbulence are weak, the behavior of the turbulent meltwater plume plays a key role in determining melting rates.

The dynamics of meltwater flows depend on several factors, including ocean stratification and variation of the pressure-dependent freezing temperature with depth, which both impose preferred length scales on the system [*Lane-Serff*, 1995; *Jenkins*, 2011]. When the meltwater flow rises in a stratified ocean, ambient waters of high density are entrained at depth, and the mixture is carried upward to regions of lower ambient density by the buoyant meltwater flow. When the rising mixture reaches and exceeds its neutral density level, the upward buoyancy force is lost and reverses sign. The plume then decelerates, before separating from the ice surface and intruding into the background stratification. These dynamics are broadly similar to the intrusion of turbulent atmospheric plumes into a stratified environment [*Morton et al*., 1956] and have been observed in corresponding models of turbulent meltwater plumes [*Jenkins*, 1993; *Lane-Serff*, 1995; *Jenkins*, 2011] and ocean observations, as discussed below. When a vertical ice face melts into a salinity gradient, further melting can occur above the intrusion level to restart the process, with laboratory experiments for laminar or weakly turbulent flow showing a repeating series of layered intrusions [*Huppert and Turner*, 1978, 1980]. *Huppert and Turner* [1978] and *Jacobs et al*. [1981] argued that this mechanism was consistent with observations of layered staircase structures seen in the ocean stratification near icebergs and the Erebus ice tongue, and similar layered intrusions have been modeled under ice shelves [*Jenkins*, 1993]. More recent oceanographic measurements provide evidence of mid-depth intrusions near tidewater glaciers in certain Greenland fjords [e.g., *Straneo et al*., 2011] which are qualitatively consistent with predictions of an ocean circulation model [*Sciascia et al*., 2013]. Such intrusive flows have important implications for the density and water properties of outflows that contribute to ocean circulation [*Straneo et al*., 2011; *Straneo and Cenedese*, 2015]. We will here focus on quantifying the key features of turbulent plumes at a melting ice face in a stratified fluid.

An alternative dynamical constraint on meltwater plumes arises due to variation of the freezing point temperature with depth [e.g., *Lewis and Perkin*, 1986]. For flow over large vertical scales, such as under the large Antarctic ice shelves, the freezing temperature is significantly depressed at depth and favors enhanced melting. As a meltwater plume rises toward the ocean surface the in situ freezing point temperature increases and the rising plume water may become supercooled, resulting in basal freezing or marine ice accumulation. This "ice-pump" mechanism [*Lewis and Perkin*, 1986] can lead to a significant vertical redistribution of ice shelf mass in some settings [e.g., *Jenkins*, 1991; *Jenkins and Bombosch*, 1995].

A variety of modeling approaches have been applied to study meltwater flows under ice shelves and at glacier termini. Ocean general circulation models [see *De Rydt et al*., 2014; *Straneo and Cenedese*, 2015, for recent summaries] provide key insights into the complex interaction of meltwater flow with the background ocean, but place stringent requirements on resolution to faithfully characterize the meltwater flow and turbulent entrainment inside an $O(10\,\mathrm{m})$ boundary layer next to the ice [*Xu et al*., 2012; *Sciascia et al*., 2013; *Xu et al*., 2013; *Kimura et al*., 2014; *Slater et al*., 2015]. An alternative approach applies a simplified plume model, which uses conservation laws averaged over the width of the meltwater plume to provide a computationally efficient characterization of flow in directions along the ice face [see, e.g., *Jenkins*, 1991; *Payne et al*., 2007; *Jenkins*, 2011]. Plume models require the background stratification conditions to be specified a priori, but do provide a convenient tool for characterizing melting rates and flow in settings where the background conditions evolve on longer timescales than the plume and can be treated as quasi-steady. *Cowton et al*. [2015] have recently coupled a plume model for strong subglacially fed plumes to the evolving stratification in an ocean circulation model. A third approach uses simple empirically motivated parameterizations of melting when it is not desirable to use a full dynamical model for ocean flow. Key examples include ice-sheet flow models [e.g., *Walker et al*., 2008; *Pollard*, 2009] run over centennial and millenial timescales that are long compared with the faster local ocean dynamics, or for outlet glaciers melting in narrow fjords of order 10 km width which are challenging to resolve fully.

A key goal of the present study is to use a more detailed plume model to derive scaling laws for meltwater plume dynamics in a linearly stratified fluid, suitable for application as part of a parameterization in larger-scale models, or as a tool that can readily be applied to aid interpretation of field observations. While a linear ocean stratification is a simplifying case that is not directly applicable in some settings, it allows us to build insight into the role of stratification on meltwater flow. Moreover, the solutions derived also capture the leading-order dynamics for nonlinear stratifications that vary slowly compared with the characteristic length scale for linearly stratified flow, and can thus be regarded as locally linear. In these circumstances, one might approximate melt rates from a piecewise-linear reconstruction of the stratification.

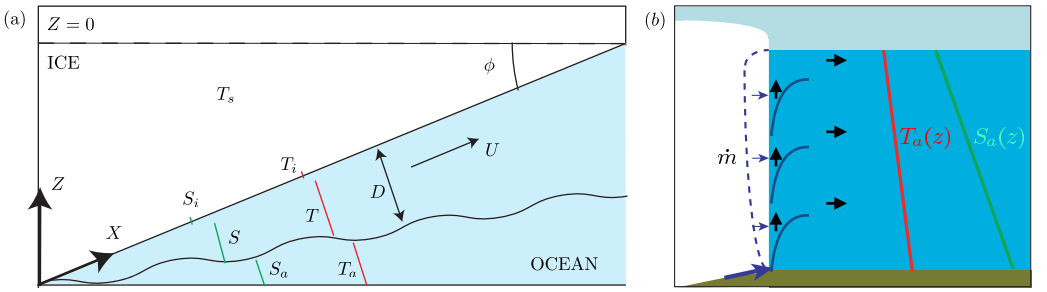

Figure 1. (a) Schematic illustration of model geometry for an ice shelf inclined at angle ϕ to the horizontal. The plume width D, velocity U, salinity S, and temperature T vary with along slope distance X (or equivalently vertical coordinate Z which increases upward). Subscripts a and i denote ambient and interface properties, respectively. (b) For ice melting at rate $\dot{m}$ into a strongly stratified fluid with ambient temperature $T_a(Z)$ and salinity $S_a(Z)$, the rising flow can pass a neutral buoyancy level and intrude into the ambient, with a new flow starting above the intrusion leading to the formation a series of layered intrusions.

We outline the plume model for meltwater flow in section 2, relevant to both vertical calving faces and sloping ice shelves. In section 3, analytical solutions are determined for meltwater flow in an unstratified ocean (section 3.1) that motivate a nondimensionalization and approximation that captures the leading-order scalings in a linearly stratified ocean (section 3.2). The latter scalings are tested via comparison to numerical solutions in section 4, for both vertical calving faces (section 4.3) and sloping shelves (section 4.4) and applied to case studies. In section 5, strengths and limitations are discussed, and use of the results in a parameterization is proposed, before concluding in section 6.

2. Model of Meltwater Flows

We build on the plume model of *Jenkins* [2011], which we review below for a self-contained treatment, and apply this to examine the influence of a linear ocean stratification on the plume. *Jenkins* [2011] focussed on solutions with strong subglacial discharge at the base of the glacier, relevant to ice sheets with strong surface melt and an active subglacial drainage network. In this study, we focus on an alternative configuration where the initial subglacial discharge is dynamically negligible, and the primary buoyancy is derived from melting of the submerged ice face. Regions of low subglacial discharge will occur for many Antarctic ice shelves, and for Greenland glaciers in winter when there is a negligible supply of surface melt to feed the subglacial drainage system. Furthermore, these conditions are also relevant in summer to regions of the ice face between strong buoyancy sources from localized subglacial drainage channels, or if the initial meltwater plume intrudes into the stratified ambient and a new meltwater flow develops next to the ice face above. For example, *Cowton et al*. [2015] identified that the volume of such background melt is potentially comparable to melting controlled by localized subglacial plumes. As such, the results presented here for low initial buoyancy fluxes are complementary to those derived by *Jenkins* [2011] for large subglacial discharge. We also note that while *Jenkins* [2011] conducted calculations with a simplified approximation to the interfacial conditions, we here retain salinity-dependent interface dynamics.

2.1. Outline of Plume Model

Following *Jenkins* [2011], we build insight by considering a meltwater flow adjacent to a locally planar region of ice face inclined at an angle ϕ to the horizontal, as illustrated in Figure 1. As a simplifying assumption to allow a tractable analysis, we do not solve a full free boundary problem for the evolving ice geometry, but instead use solutions for a locally flat region of the ice surface to infer the tendency for melting relevant to small deformations of an initially planar region of the interface (in line with many previous approaches, such as *Jenkins* [2011]). This leads to an effectively one-dimensional meltwater plume model that applies following ocean flowlines under the locally planar region of ice surface. The potential for application of the results to regions of ice face with weak horizontal curvature is discussed later in section 5.3.3. We also neglect coriolis forces. Hence the results will be most relevant to vertical ice faces, or to sloping ice shelves either on scales much smaller than the Rossby deformation radius, or where geometrical

confinement results in an effectively one-dimensional flow along streamlines. The ice sheet or shelf is assumed to have uniform salinity $S_s \approx 0$ and temperature T_s far into the ice interior, and is in contact with an ocean with stratified ambient temperature $T_a(Z)$, salinity $S_a(Z)$, and density $\rho_a(Z)$ that vary with depth characterized by vertical coordinate Z (positive upward). For simplicity, we assume that variations in T_s are small over the characteristic flow scales identified later. We employ an extended Boussinesq approximation with constant reference density ρ_l in the liquid, except in the buoyancy force where the density ρ is multiplied by the gravitational acceleration g. We also assume that all other material properties are constant in each phase, with solid density ρ_s, and heat capacities c_s and c_l for solid and liquid phases, respectively. Melting generates a buoyant plume with mean alongslope velocity U, mean temperature T, mean salinity S, and density ρ over an effective width D.

We seek quasi-steady solutions for development of flow with distance $X=(Z-H)/\sin\phi$, where $|H|$ is the depth below the ocean surface at which flow is initiated. Conservation of mass shows that the alongslope mass flux increases either by entrainment of ambient fluid at rate $\dot{e}$ or addition of meltwater at rate $\dot{m}$, yielding

$$\rho_l \frac{d}{dX}(DU)=(\dot{e}+\dot{m})\rho_l. \tag{1}$$

The turbulent entrainment rate is parameterized as a linear function of velocity

$$\dot{e}=E|U|, \tag{2}$$

where $E=E_0\sin\phi$, E_0 is a constant entrainment coefficient and the $\sin\phi$ factor is introduced to emulate observations that entrainment is reduced when it involves the potential energy cost of a vertical component of flow lifting dense fluid into the plume. Whilst alternative Richardson number-dependent entrainment parameterizations have been proposed, the exact form remains under debate [see e.g., *Wells et al*., 2010] and so we here focus primarily on a simple form motivated by field observations [*Bo Pedersen*, 1980; *Hughes and Griffiths*, 2006] and laboratory experiments [*Wells and Wettlaufer*, 2005]. Such a parameterization has commonly been used in a range of earlier studies of meltwater plumes and ocean density currents [see *Jenkins*, 1991; *Wells and Wettlaufer*, 2007; *Jenkins*, 2011, for a selection of examples]. In the supporting information section S1, we also consider the impact on the along-flow structure from using one of two alternative entrainment formulations that depend on the Richardson number [*Kochergin*, 1987; *Wells et al*., 2010] for a selection of case studies. For unstratified flow, we find that both of these parameterizations recover a constant entrainment coefficient, which scales as $E \propto \sin\phi$ under shallow ice-shelf slopes. For stratified flow, we find that the solution method described below can be extended to use entrainment functions that depend on a local Richardson number, which yield qualitatively similar along-slope variation of the flow in the case studies considered. Note also that in line with several previous studies of meltwater plumes [see *Jenkins*, 2011, and references therein] we have neglected the possibility of continuous detrainment along the flow—this assumption is discussed further in sections 5.3.5 and supporting information S2.

Conservation of momentum shows that the alongslope momentum flux changes under the action of buoyancy forces and shear stress τ_l from the solid ice face

$$\frac{d}{dX}(DU^2)=g\sin\phi D\left(\frac{\rho_a-\rho}{\rho_l}\right)-\frac{\tau_l}{\rho_l}, \tag{3}$$

where g is the gravitational acceleration. We have neglected a term describing alongslope gradients in hydrostatic pressure, which is reasonable for flows that are supercritical with respect to the relevant gravity wave speed. Note that we have here defined the depth integrated density deficit as $D(\rho_a-\rho)$ consistent with *Jenkins* [2011]. Alternative definitions are possible (such as replacing ρ_a with the average of the ambient density over the depth of the plume) which recover the same leading-order behavior to within the accuracy of the boundary-layer approximation used in deriving the plume model (which assumes that the plume is thin compared to along flow length scales).

The temperature and salinity in the plume are determined from conservation of thermal energy and salt, considering contributions from alongslope advection, entrainment of ambient fluid, input of meltwater, and turbulent fluxes of heat q_l, and salt r_l to the ice ocean interface. This results in

$$\rho_l c_l \frac{d}{dX}(DUT) = \dot{e}\rho_l c_l T_a + \dot{m}\rho_l c_l T_i - q_l, \tag{4}$$

$$\rho_l \frac{d}{dX}(DUS) = \dot{e}\rho_l S_a + \dot{m}\rho_l S_i - r_l, \tag{5}$$

where T_i is the temperature at the ice-ocean interface and S_i is the interfacial salinity. The parameterization of the turbulent fluxes τ_l, q_l, and r_l is discussed later.

The ice-ocean interface moves with normal velocity V measured relative to any motion of the ice (where $V < 0$ for melting), with mass conservation across the interface requiring

$$\rho_l \dot{m} = -\rho_s V. \tag{6}$$

The melting rate V is determined by considering conservation of energy across the ice-ocean interface

$$\rho_s L V = q_s - q_l, \tag{7}$$

where L is the latent heat of fusion and q_s is the heat flux from the solid. A boundary layer approximation for thermal diffusion in the ice results in

$$q_s = -\rho_s c_s (T_i - T_s) V, \tag{8}$$

(see appendix of *Wells and Worster* [2011], or *Sergienko et al*. [2013] for example). The ice-ocean interface lies at the in situ freezing temperature, which depends on salinity and pressure. We assume this liquidus function $T_L(S, p)$ can be approximated by the linear relationship

$$T_i = T_L(S_i) \equiv T_m + \lambda Z - \Gamma(S_i - S_s) \tag{9}$$

where T_m, Γ, and λ are all constants for a given S_s, where we will here use $S_s \approx 0$. The coefficient λ approximates the rate of variation of freezing temperature with depth as a result of linearizing the Clausius-Clapeyron relation for phase coexistence, with the background hydrostatic pressure increasing with depth. The interfacial salinity S_i is determined from conservation of salt at the ice-ocean interface during melting, yielding

$$\rho_s (S_i - S_s) V = -r_l. \tag{10}$$

Finally, we assume that the density differences that give rise to buoyancy forces are well approximated by a linearized equation of state, so that

$$\rho - \rho_a = \rho_l [\beta(S - S_a) - \alpha(T - T_a)], \tag{11}$$

where α and β are constant.

The turbulent fluxes of momentum, salt, and heat at the ice-ocean interface depend on the detailed turbulent boundary layer dynamics, and are a source of uncertainty in the present modeling framework. An analysis of purely thermal flows next to an impermeable heated surface suggests two possible regimes of turbulent heat transfer depending on whether the breakdown of the viscous sublayer is controlled by the intrinsic buoyancy of the sublayer, or by the shear exerted by the main body of the turbulent plume [*Wells and Worster*, 2008]. The transition between the two regimes is characterized by an appropriate Reynolds number for the viscous sublayer, with the former buoyancy-controlled regime occurring for smaller Reynolds numbers, and the latter shear-driven regime becoming significant for stronger flows that attain a critical Reynolds number criterion [see *Wells and Worster*, 2008, for further details]. The buoyancy-controlled regime predicts heat flux scaling laws consistent with laboratory-scale experiments for flows in air, and ice melting in saltwater [*Kerr and McConnochie*, 2015] while the turbulent flux scaling laws for the shear-driven regime are dynamically similar to those that have been widely used in ice shelf water plume models on larger geophysical scales [see e.g., *Jenkins*, 1991; *Jenkins et al*., 2010; *Jenkins*, 2011, and derivatives thereof]. An extension of the analysis to two-component flows with ice melting into a warm saline ocean produces similar dynamical regimes [*Wells*, 2008], but there is currently insufficient experimental or observational data to constrain the relevant transition scales for the combined heat and salt transfer when ice melts into water. In light of the uncertainties over the range of conditions for which the buoyancy-controlled sublayer dynamics are dominant, we will primarily focus on results relevant to a shear-dominated viscous sublayer

that have been widely assumed in many previous models. In this limit, we assume that the turbulent fluxes of heat and salt to the ice-ocean interface can be approximated by

$$q_I = \rho_I c_I \mathrm{St} |U| (T - T_i), \tag{12}$$

$$r_I = \rho_I \mathrm{St_m} |U| (S - S_i), \tag{13}$$

for constant heat transfer coefficient St and salt transfer coefficient $\mathrm{St_m}$. We also approximate turbulent shear stresses by the quadratic drag law

$$\tau_I = \rho_I \mathrm{C_d} U |U|, \tag{14}$$

with a constant drag coefficient $\mathrm{C_d}$. In the supporting information, we present details of a corresponding calculation using a scaling law for dissolution rates of a vertical ice surface with a buoyancy-driven viscous sublayer. The regime with a buoyancy-driven viscous sublayer yields qualitatively similar flow structure to the case with a shear-driven sublayer considered in the main text but with some quantitative differences in the scalings obtained.

2.2. Reformulation Using Density Deficit and Thermal Driving

A key insight in the work of *Jenkins* [2011] was to recast (1)–(11) in terms of the thermal driving

$$\Delta T = T - T_L(S) \equiv T - T_m - \lambda Z + \Gamma (S - S_s), \tag{15}$$

and the density deficit

$$\Delta \rho = \rho_a - \rho. \tag{16}$$

Jenkins [2011] combined these expressions with a simplified approximation to the interfacial thermodynamics to derive a simplified plume model. Our preliminary analysis suggested that the modified interfacial conditions made a small but nonnegligible modification to the scalings (accounting for the full salinity-dependent interface thermodynamics modifies the melt rates and layer scales by around 10–30% for $-1^\circ\mathrm{C} \leq T_a \leq 4^\circ\mathrm{C}$ and $S_a = 35\ \mathrm{g\ kg^{-1}}$.) Thus we here maintain the full three-equation formulation (7), (9), and (10) for interface dynamics that explicitly accounts for interfacial salinity. We define a dimensionless melt rate factor M satisfying

$$\dot{m} = M |U|. \tag{17}$$

This departs from the analysis of *Jenkins* [2011] who used the alternative definition $\dot{m} = M_0 \Delta T |U|$, with constant M_0, but we here use (17) for notational convenience in anticipation of a more complex temperature dependence when using salinity-dependent interfacial thermodynamics.

After some algebra (1)–(5) can be rewritten as

$$\frac{d}{dX}(DU) = E|U| + M|U|, \tag{18}$$

$$\frac{d}{dX}(DU^2) = g \sin\phi D \Delta\rho - \mathrm{C_d} U |U|, \tag{19}$$

$$\frac{d}{dX}\left(DU\frac{\Delta\rho}{\rho_I}\right) = \frac{1}{\rho_I}\frac{d\rho_a}{dX} DU + \frac{\Delta\rho_i^{ef}}{\rho_I} M|U|, \tag{20}$$

$$\frac{d}{dX}(DU\Delta T) = \Delta T_a E|U| + M|U|\left[T_i^{ef} - T_L(S_s)\right] - \lambda \sin\phi DU. \tag{21}$$

where $\Delta T_a = T_a - T_L(S_a)$. Following *Jenkins* [2011], we have also defined an effective temperature of released meltwater

$$T_i^{ef} = T_i - \frac{L}{c_I} + \frac{c_s}{c_I}(T_s - T_i), \tag{22}$$

which accounts for the heat required to warm the solid to the melting temperature and the subsequent latent heat required for melting, and an effective meltwater density difference

$$\Delta\rho_i^{ef} = \rho_l\left[\beta(S_a - S_s) - \alpha\left(T_a - T_i^{ef}\right)\right]. \tag{23}$$

The interfacial temperature T_i and melt rate factor M are determined using the three-equation formulation for interface thermodynamics (7), (9), and (10). We use (6) and (17) to express V in terms of M. Combining (7)–(10), (12)–(13), and eliminating T_i and S_i results in a quadratic equation $aM^2 + bM + c = 0$ for M, where

$$\begin{aligned} a &= 1 - \frac{c_s}{L}[T_s - T_L(S_s)], \\ b &= \mathrm{St}_m\left\{1 - \frac{c_s}{L}[T_s - T_L(S)]\right\} - \mathrm{St}\frac{c_l}{L}[T - T_L(S_s)], \\ c &= -\mathrm{St}_m\mathrm{St}\frac{c_l}{L}[T - T_L(S)], \end{aligned} \tag{24}$$

depend on X via the local plume temperature T, salinity S, and depth-dependent freezing temperature $T_L(S_s)$. The physically meaningful root has positive melting rate for positive thermal driving, and the melt-rate factor and interfacial temperature satisfy

$$M = \frac{-b + \sqrt{b^2 - 4ac}}{2a}, \qquad T_i = T_L(S_s) - \Gamma(S - S_s)\frac{\mathrm{St}_m}{M + \mathrm{St}_m}. \tag{25}$$

Note that because S and T are determined from the plume equations (18–21) which depend on T_i, the solutions (25) are implicitly defined. The latter expression for T_i illustrates that the salinity-dependent freezing temperature depends on the competition between the release of freshwater by melting at rate $M|U|$ and the turbulent transport of salt to the interface at rate $\mathrm{St}_m|U|$. As a result of this freezing point depression, the melt rate factor depends in principle on both the rate of heat transfer and the rate of salt transfer to the ice-ocean interface (illustrated by the dependence of M on both St_m and St). When calculating values of M and T_i, the expressions

$$\Gamma(S - S_s) = \frac{\beta(S_a - S_s) - \alpha(T_a - T_L(S_s)) + \alpha\Delta T - \Delta\rho/\rho_l}{\alpha + \beta/\Gamma}, \tag{26}$$

$$T = T_L(S_s) + \Delta T - \Gamma(S - S_s), \tag{27}$$

are useful, which result from a rearrangement of (11), (15), and (16).

3. Analytical Results: Scalings for Flow Development

In this section, we develop simple solutions in special cases, motivating a nondimensionalization of the governing equations that allows us to identify key simplifications relevant to stratified flows.

3.1. Flow in a Warm Unstratified Ambient Ocean: Weak Subglacial Discharge

To build initial insight into relevant flow scalings, we first consider cases with an unstratified ambient ocean of uniform temperature and salinity ($d\Delta\rho_a/dX = dT_a/dX = dS_a/dX = 0$), and where the pressure-dependent variation of freezing point with depth is small and can be neglected ($\lambda = 0$). The ambient thermal driving, effective meltwater temperature, and effective meltwater density difference are therefore all constant and equal to their initial values which we define as

$$\Delta T_{a0} = \Delta T_a|_{X=0}, \quad \Delta T_{i0}^{ef} = \left[T_i^{ef} - T_L(S_s)\right]_{X=0}, \quad \Delta\rho_{i0}^{ef} = \Delta\rho_i^{ef}|_{X=0}.$$

When the initial subglacial discharge at $X = 0$ is negligible, the equations ((18–25)) admit self-similar power law solutions

$$D = D_u(X) \equiv \frac{2}{3}(E + M_u)X, \tag{28}$$

$$\Delta T = \Delta T_u \equiv \frac{\Delta T_{a0}E + \Delta T_{i0}^{ef}M_u}{E + M_u}. \tag{29}$$

$$\Delta\rho=\Delta\rho_u \equiv \frac{M_u}{E+M_u}\Delta\rho_{i0}^{ef}, \tag{30}$$

$$U=U_u(X) \equiv \left[\frac{2(E+M_u)}{3C_d+4(E+M_u)}\right]^{1/2}\left(\frac{\Delta\rho_u}{\rho_l}g\sin\phi\, X\right)^{1/2}, \tag{31}$$

$$\dot{m}=M_u U_u(X) \tag{32}$$

where the constant value of the melt rate factor $M = M_u$ is determined implicitly using (24) and (25), after expressing T and S in terms of (30) and (29). Hence the expressions in (28)–(32) carry an implicit dependence on the turbulent heat and salt transfer coefficients St and St_m, through their impact on the melt rate factor M_u.

The above solutions show that entrainment of ambient fluid and mass input by melting lead to a linear increase of the plume width D with distance X alongslope in (28). A constant thermal driving in the plume ΔT arises in (29) as a mixing ratio from the balance of entrainment of ambient waters with ambient thermal driving ΔT_{a0} and the release of meltwater with the effective temperature difference ΔT_{i0}^{ef}. Likewise, the plume density deficit in (30) arises as a mixing ratio between meltwater released with effective density deficit $\Delta\rho_{i0}^{ef}$ and the entrainment of ambient fluid (which has no density deficit compared to the background ocean). The density deficit in turn provides buoyancy to drive a flow that accelerates along the slope, moderated by turbulent drag and the increase in plume volume along slope.

A simplified approximation to the melt rate can be derived by firstly noting that $L/c_s \approx 160^{\circ}$C, and hence

$$\frac{c_s[T_s-T_L(S_s)]}{L} \ll 1, \qquad \text{and} \qquad \frac{c_s\Gamma(S_{a0}-S_s)}{L} \ll 1, \tag{33}$$

are well satisfied unless the ice temperature T_s is very low (where $S_{a0}=S_a|_{X=0}$). Similarly, we assume that $c_l[T_i-T_L(S_s)]/L \ll 1$ and $c_s[T_i-T_s]/L \ll 1$ so that $\Delta T_{i0}^{ef} \approx -L/c_l$ is dominated by the latent heat term at leading order. We also assume that $M_0 \ll E$ (which can be checked a posteriori). In Appendix A, we show that these approximations combine with the solution (28)–(32) to yield

$$M_0=\frac{1}{2}\left\{\frac{E\mathrm{St}}{(E+\mathrm{St})}\frac{c_l[\Delta T_{a0}-\Gamma(S_{a0}-S_s)]}{L}-\mathrm{St_m}\right\}+\ldots$$
$$+\frac{1}{2}\sqrt{\left\{\frac{E\mathrm{St}}{(E+\mathrm{St})}\frac{c_l[\Delta T_{a0}-\Gamma(S_{a0}-S_s)]}{L}+\mathrm{St_m}\right\}^2+\frac{4\mathrm{St_m}E\mathrm{St}}{(E+\mathrm{St})}\frac{c_l\Gamma(S_{a0}-S_s)}{L}} \tag{34}$$

We also show in Appendix A that this nonlinear function of T_a asymptotes to the limit

$$M_0 \sim \frac{E\mathrm{St}}{(E+\mathrm{St})}\frac{c_l\Delta T_{a0}}{L} \qquad \text{for} \quad \Delta T_{a0} \gg \Gamma(S_{a0}-S_s), \tag{35}$$

relevant to large thermal driving. The scaling (35) has a straightforward physical interpretation by making an analogy with the conductance of electrical resistors in series (with conductance being inversely proportional to resistance). The rate of heat transfer to the ice face depends on the product of available thermal energy per unit volume $\rho_l c_l \Delta T_{a0}$ and the effective conductance of heat transfer across the plume (in the same way that electrical current depends on the voltage and net conductance across a circuit). For the meltwater plume, heat must first be transferred into the plume with effective conductance $E|U|$ controlled by turbulent entrainment, before transferring heat from the plume interior across the viscous sublayer to the ice face with a conductance $\mathrm{St}|U|$ controlled by turbulent heat transfer. The net resistance of resistors in series is given by the sum of individual resistances. Hence, noting that conductance is inversely proportional to resistance, the net conductance is proportional to $(1/E+1/\mathrm{St})^{-1}$ which yields the prefactor in (35) that controls heat transfer. The melt rate factor M_0 is then determined by the ratio of heat supplied across the boundary layer compared with the latent heat required to melt.

Incorporating the scaling (35) for M_0 into (32) and noting that $M_0 \ll E$ by assumption, the dimensional melt rate is approximately

$$\dot{m} \sim \left(\frac{c_p \Delta T_{a0}}{L}\right)^{3/2} \left(\frac{E\mathrm{St}}{E+\mathrm{St}}\right)^{3/2} \left(\frac{2E}{4E+3\mathrm{C_d}}\right)^{1/2} \left(\frac{g \sin\phi \Delta\rho_{i0}^{ef}}{\rho_l} X\right)^{1/2}$$

$$\text{for} \quad \Delta T_{a0} \gg \Gamma(S_{a0} - S_s). \tag{36}$$

Thus, the melting rate scales as the 3/2-power of thermal driving for strong thermal drivings (i.e., significantly larger than 2°C for typical ocean conditions) with a more complex dependence for smaller thermal drivings. The nonlinear dependence of melt rate with thermal driving results from the rate of heat transfer depending on the heat available for melting (which scales linearly with ΔT_{a0}), but also on the strength of the turbulent flow. The velocity U is temperature-dependent because it depends on the supply of buoyant melt from the ice face.

3.2. Stratified Flow: Nondimensionalization

Such self-similar solutions arise because there is no dynamically relevant length scale imposed on the system that effects the initial development of the flow. However, the presence of a nonnegligible background density stratification $\partial\rho_a/\partial X$ introduces a new length scale

$$l_\rho = \Delta\rho_u \left|\frac{\partial\rho_a}{\partial X}\right|^{-1}, \tag{37}$$

where $\Delta\rho_u$ is given by evaluating the unstratified density scale (30) at the origin of the flow $X = 0$. This stratification length-scale l_ρ represents the alongslope distance that a parcel of initial density deficit $\Delta\rho_u$ must travel to reach its neutral buoyancy level within the ambient density stratification, and we will see that it is the characteristic length scale when a repeating layered flow forms. We now show that by nondimensionalizing variables, and making a few restrictions on the range of stratifications considered, we can determine approximate scalings for stratified flow, that capture the leading order behavior of full numerical solutions across a broad range of ocean conditions. We introduce a dimensionless distance $x = X/l_\rho$. Characteristic scales for the stratified system are obtained by evaluating the unstratified similarity solutions (28)–(32) at the stratification length-scale $X = l_\rho$. This leads to the definition of dimensionless versions of the plume width b, plume velocity u, density deficit χ, thermal driving θ, and melt rate factor μ according to

$$\Delta\rho = \Delta\rho_{i0}^{ef} \frac{M_0}{E+M_0}\chi, \qquad \Delta T = \frac{\Delta T_{a0}E + \Delta T_{i0}^{ef} M_0}{E+M_0}\theta, \qquad D = \frac{2}{3}(E+M_0) l_\rho b,$$

$$U = \left[\frac{2(E+M_0)}{3\mathrm{C_d}+4(E+M_0)}\right]^{1/2} \left(\frac{\Delta\rho_u}{\rho_l} g \sin\phi\, l_\rho\right)^{1/2} u, \qquad \dot{m} = M_0 U_u(l_\rho)\, \mu u, \tag{38}$$

where $M_0 = M_u(l_\rho)$ is consistent with the unstratified solution (32). Substituting (38) into the plume equations (18–21) results in the dimensionless system

$$\frac{d}{dx}(bu) = \frac{3}{2}|u|\left[1 + \frac{M_0}{E+M_0}(\mu - 1)\right], \tag{39}$$

$$\frac{d}{dx}(bu^2) = \left[\frac{3\mathrm{C_d}}{2(E+M_0)} + 2\right] b\chi - \frac{3\mathrm{C_d}}{2(E+M_0)} u|u|, \tag{40}$$

$$\frac{d}{dx}(bu\chi) = \frac{3}{2}\left(\frac{\Delta\rho_i^{ef}}{\Delta\rho_{i0}^{ef}}\right)\mu|u| - bu, \tag{41}$$

$$\frac{d}{dx}(bu\theta) = \frac{3}{2}|u|\left[1 + \left(\frac{E\Delta T_a + M_0 \Delta T_i^{ef}\mu}{E\Delta T_{a0} + M_0 \Delta T_{i0}^{ef}} - 1\right)\right] - \frac{l_\rho \lambda \sin\phi}{\Delta T_u} bu, \tag{42}$$

where μ satisfies

$$aM_0^2\mu^2 + bM_0\mu + c = 0, \tag{43}$$

with a, b, and c given by (24). By construction, the unstratified solution has $\mu = 1$. The system (39)–(43) still contains significant dependence on the imposed thermal and salinity conditions through ΔT_a, ΔT_i^{ef}, $\Delta\rho_i^{ef}$, and implicitly through M_0. However, this dependence is removed at leading order if the following conditions hold

$$\frac{M_0}{E} \ll 1, \qquad \epsilon_{\Delta T} \equiv \left(\frac{E\Delta T_a + M_0 \Delta T_i^{ef}}{E\Delta T_{a0} + M_0 \Delta T_{i0}^{ef}} - 1\right) \ll 1,$$
$$\epsilon_{\Delta\rho} \equiv \left(\frac{\Delta\rho_i^{ef}}{\Delta\rho_{i0}^{ef}} - 1\right) \ll 1, \qquad \epsilon_\lambda \equiv \frac{l_\rho \lambda \sin\phi}{\Delta T_u} \ll 1, \qquad |\mu - 1| \ll 1. \tag{44}$$

The first four of these conditions can be estimated a priori based on the imposed stratification conditions over the stratification-scale l_ρ. We here focus on cases where stratification is significant, and Table 1 describes representative values for the upper 200m in a selection of Greenland fjords, where the ocean is typically strongly stratified. The first condition in (44) requires that the volume of fluid introduced by melting is small compared with that entrained from the ambient. Because the ratio $L/c_l \approx 80^\circ$C is usually significantly larger than temperature differences in the neighboring ocean, we can approximate $\Delta T_i^{ef} \approx -L/c_l + c_s(T_s - T_m)/c_l$ which is constant at leading order. Hence the second and third conditions are satisfied if the along flow variations in the thermal driving ΔT_a and effective meltwater density contrast $\Delta\rho_{i0}^{ef}$ are both small compared to their respective initial values. The fourth condition requires that variations in the pressure-dependent freezing temperature over the depth of a layer are small compared with the characteristic thermal driving ΔT_u. The fifth condition is an assumption on part of the solution μ, and must be verified a posteriori. From the comparison to numerical results, we find that all of the conditions (44) hold to a good approximation for strongly stratified conditions relevant to Greenland fjords with negligible subglacial discharge, as discussed later in section 4.

Applying the approximations in (44), we obtain the simplified dimensionless system

$$\frac{d}{dx}(bu) = \frac{3}{2}|u|, \quad \frac{d}{dx}(bu^2) = (2+\gamma)b\chi - \gamma u|u|, \quad \frac{d}{dx}(bu\chi) = \frac{3}{2}|u| - bu, \quad \frac{d}{dx}(bu\theta) = \frac{3}{2}|u|. \tag{45}$$

There is now only a single parameter $\gamma = C_d/E$ which is a constant for any fixed slope angle ϕ. In the case of negligible subglacial discharge, appropriate initial conditions are

$$bu = 0, \qquad bu^2 = 0, \qquad bu\chi = 0, \qquad bu\theta = 0. \tag{46}$$

Note that strong subglacial discharge would introduce new scalings into the initial conditions, which are not accounted for here. When the approximations (44) are accurate, this reduced dimensionless model represents a major simplification, because it demonstrates that for a chosen γ the leading order flow profiles and melting patterns have a universal shape for all imposed conditions, described by the unique solution to (45)–(46). The relative magnitudes of plume flow and melt can then be determined by combining the dimensional scaling factors with the universal shape, according to (38). This allows us to deduce robust scaling laws for the amplitude of the melt rate and flow properties.

4. Numerical Results

We complement the key analytical results in section 3, with numerical solutions of the full ordinary differential equation system (18)–(25) and of the simplified system (45) to test the viability of these scalings.

4.1. Numerical Method

Numerical solutions were obtained using a standard routine for solving stiff systems of ordinary differential equations using adaptive space-stepping (function "ode15s" in the MATLAB software package), to allow for the possibility of rapid adjustments from the initial conditions in a boundary layer near $x = 0$. The simplified system (45)–(46) forms a standard initial value problem for the dimensionless fluxes $\mathbf{y} = [bu, bu^2, bu\chi, bu\theta]$. For the full system (39)–(43), the corresponding initial value problem for the dimensional fluxes is solved with the interfacial constraints imposed using an iterative root finding algorithm to determine M and T_i in terms of the known quantities at each space-step. For sufficiently strong stratifications, we observed that the flow often develops intrusions where the plume decelerates to zero velocity, with mass conservation resulting in a numerical singularity where the plume width diverges. An intrusion was identified and the integration halted when the plume velocity falls below a small threshold $u < u_{thresh}$ for each system, with values $u_{thresh} < 10^{-4}$ yielding quantitatively consistent results. If an intrusion forms at some depth $Z = H_n$, heat transfer and melting of the overlying ice face will continue to drive flow and so we restart the integration with a new layer of flow at the revised origin $X = (Z - H_n)/\sin\phi$ and repeat this process until the flow

Table 1. Characteristic Values of the Parameter Groupings Identified in (44) Based on Temperature and Salinity Profiles Measured in Six Greenland Fjords[a]

Glacier	Z (m)	T_a (°C)	S_a (g kg^{-1})	dT_a/dZ (°C m^{-1})	dS_a/dZ (g kg^{-1} m^{-1})	M/E	$\lvert\epsilon_{\Delta T}\rvert$	$\lvert\epsilon_{\Delta\rho}\rvert$	$\lvert\epsilon_{\lambda}\rvert$
79NG	−100	−1.16	33.94	−0.068	−0.061	0.0002	0.0079	0.0002	0.0001
	−200	0.34	34.50	−0.005	−0.003	0.0006	0.0132	0.0006	0.0018
KG	−100	−0.26	33.12	−0.015	−0.023	0.0004	0.0051	0.0004	0.0002
	−200	0.39	34.22	−0.004	−0.003	0.0006	0.0130	0.0006	0.0021
HG	−100	−0.50	33.01	−0.003	−0.006	0.0003	0.0048	0.0003	0.0008
	−200	2.22	33.94	−0.038	−0.011	0.0011	0.0319	0.0011	0.0006
JI	−100	1.58	33.22	−0.008	−0.007	0.0009	0.0093	0.0009	0.0008
	−200	2.25	33.96	−0.003	−0.007	0.0011	0.0042	0.0011	0.0008
TF	−100	1.20	33.15	−0.005	−0.011	0.0008	0.0046	0.0008	0.0005
	−200	1.02	33.73	0.012	−0.006	0.0007	0.0113	0.0007	0.0008
PG	−100	−0.93	33.50	−0.012	−0.027	0.0002	0.0035	0.0002	0.0002
	−200	−0.23	34.56	−0.004	−0.005	0.0004	0.0077	0.0004	0.0011

[a]79 North Glacier: 79NG; Kangerdlugssuaq: KG; Hellheim Glacier: HG; Jakobshavn Isbrae: JI; Torssukatak Fjord: TF; Petermann Glacier: PG. Stratification values are approximated at two representative depths of 100m and 200 m using data from Figure 3 of *Straneo et al.* [2012], from which the scales in (44) are evaluated using a characteristic length scale $X=l_\rho$ and $\sin\phi=1$.

reaches the end of the integration domain at some specified Z. Our focus in this paper is on flows generated by melting of the submerged ice face, with negligible subglacial discharge. Thus the initial conditions in each new layer were usually determined by evaluating the dimensionless form of the similarity solution (28)–(31) at a small distance $x=10^{-4}$ above the start of the new layer, which corresponds to a leading-order Frobenius series solution valid for small x. Corresponding dimensional quantities were used when integrating (18)–(25). Physical constants and parameter values are listed in Table 2.

4.2. Ocean Stratification Conditions

We consider numerical results for a range of dimensional background ocean temperature and salinity stratifications $T_a(z)$ and $S_a(z)$ that vary linearly with depth. We here focus on a range of stratification values motivated by examples of stratification conditions observed in Greenland fjords [*Straneo et al.*, 2012], with

$$-1.5^\circ\mathrm{C} \le T_a|_{x=0} \le 3^\circ\mathrm{C},$$

$$-0.1^\circ\mathrm{C\,m^{-1}} \le \frac{\partial T_a}{\partial Z} \le 0.1^\circ\mathrm{C\,m^{-1}}, \quad -0.1\,\mathrm{g\,kg^{-1}m^{-1}} \le \frac{\partial S_a}{\partial Z} \le -0.001\,\mathrm{g\,kg^{-1}m^{-1}}, \tag{47}$$

and $S_a|_{x=0}=35\,\mathrm{g\,kg^{-1}}$. Polar ocean observations typically show cold and fresh surface waters overlying warmer and salty water at depth, so that the density stratification is dominated by salinity variability, with $|\beta\partial S_a/\partial Z| \gg |\alpha\partial T_a/\partial Z|$. Motivated by this observation, we therefore restrict attention to simulations with $|\alpha\partial T_a/\partial Z| \le 0.1|\beta\partial S_a/\partial Z|$ in order to preserve a strongly dominant role of salinity in controlling the stratification. Over the range of T_a and S_a considered, this condition ensures that there is only modest variation in the ambient thermal driving over the stratification scale l_ρ for vertical ice faces, with $|\Delta T_a-\Delta T_{a0}|/\Delta T_{a0} < 4\%$. However, we emphasize that the present scalings break down in conditions where the ambient temperature gradient provides a leading-order control on the density stratification and (44) is no longer satisfied.

4.3. Melting of Vertical Ice Faces

We start by considering the dynamics of a single layer of flow, using the dimensionless representation to emphasize the generality of the results. Figure 2 illustrates variation of the flow with dimensionless distance x.

Numerical solutions of the full model (39)–(43) across an illustrative range of ambient stratification conditions (shown by colored lines) collapse well onto the solution of the reduced system (45) shown by the solid black curves in Figures 2a–2f. Hence the scalings (38) provide a good approximation to the flow across a range of ambient ocean conditions. The similarity solution (28)–(31) for an unstratified flow is also plotted as black-dashed curves in Figures 2a–2f for comparison. Figures 2g–2l show corresponding residuals given by the difference between solutions of the full model and the reduced model for each of the variables in Figures 2a–2f. The residuals are modest in magnitude compared to the full solution, except for the approach to the critical point $x=x_{int}$, where $u \to 0$ and $b \to \infty$. Small displacements of the height of this

Table 2. Physical Constants and Parameter Values[a]

Symbol	Value	Units	Description
T_s	-5	°C	Representative background ice temperature
E_0	3.6×10^{-2}		Entrainment coefficient
C_d	2.5×10^{-3}		Drag coefficient
St	1.1×10^{-3}		Heat transfer coefficient
St_m	3.1×10^{-5}		Salt transfer coefficient
Γ	5.73×10^{-2}	°C	Seawater freezing point slope
T_m	8.32×10^{-2}	°C	Freezing point offset
λ	7.61×10^{-4}	°C m^{-1}	Depth dependence of freezing point
L	3.35×10^{5}	J kg^{-1}	Latent heat of fusion for ice
c_i	2.009×10^{3}	J kg^{-1} K^{-1}	Specific heat capacity for ice
c	3.974×10^{3}	J kg^{-1} K^{-1}	Specific heat capacity for seawater
β_S	7.86×10^{-4}		Haline contraction coefficient
β_T	3.87×10^{-5}	K^{-1}	Thermal expansion coefficient
g	9.81	ms^{-2}	Gravitational acceleration

[a]Following Jenkins [2011].

critical point between the full model and reduced solutions lead to more significant deviation very close to this critical point.

The dynamics of the flow can be understood as follows. Heat transfer drives melting of the ice face, and this fresh meltwater supplies buoyancy (Figure 2c) to drive the initial acceleration of the flow along the ice face (Figure 2b). In the absence of stratification (dashed curves), the rising turbulent flow entrains dense ambient fluid, causing a linear increase in plume width (Figure 2a) along the flow. However, the nature of the mixing processes and interfacial heat and salt transfer (both parameterized proportional to the plume velocity U) and along flow advection result in a uniform density deficit and thermal driving for flow in an unstratified ambient. As discussed in section 3.1, this sustains a fixed mixing ratio of ambient waters and cold fresh meltwater of effective thermal driving ΔT_{I0}^{ef} and effective density deficit $\Delta\rho_{I0}^{ef}$, tied to the self-similar solution for the flow. By comparison, the ambient density varies with depth in a stratified flow, and this breaks the self-similar balance between entrainment and ice-ocean fluxes as water parcels are advected upward. Mixing entrains dense saline water at depth, which is advected upward along the ice face to levels with ever reducing ambient density. Thus the density deficit decreases significantly for stratified flow (Figure 2c). There is also a much slower change to the thermal driving (Figure 2d) as a result of entraining ambient waters with different temperatures at different depths. The reduced density deficit leads to a slower acceleration of the plume at middepths than in the unstratified case. Eventually the plume waters reach their neutral density within the ambient stratification, with $\Delta\rho=0$. The inertia of the vertical flow leads to an overshoot of the neutral density level, with the negative density anomaly and downward buoyancy force (Figure 2c) causing deceleration of the plume until $u\rightarrow 0$ (Figure. 2b) at a level $X=X_{int}$. Equation (18) shows that the volume flux in the plume cannot decrease with height, and so the vanishing vertical velocity $u\rightarrow 0$ generates a singular point where $b\rightarrow\infty$ and the modeling approximations break down. Physically we expect the meltwater flow to intrude into the ambient at and below the maximum rise height which we characterize by $X=X_{int}$. Determining the subsequent fate of the outflow lies beyond the scope of the plume model employed here, but we discuss possible eventualities in section 5. In addition to the maximum rise height X_{int} which sets the overall length scale of the layered flow and pattern of melting on the ice face, two other dynamically relevant scales for the intrusion and detrainment of fluid into the ambient are the scale X_{neg} where the plume first becomes negatively buoyant with $\chi(X_{neg}/l_\rho)=0$, and the subsequent neutral buoyancy level X_{neut} of plume fluid that intrudes into the ambient at the maximum rise height $X=X_{int}$. The neutral buoyancy level X_{neut} is calculated by finding $\rho(X_{int})=\rho_a(X_{neut})$. All of these scales are linearly related to the stratification scale l_ρ, with the reduced solution yielding negative buoyancy at a scale $X_{neg}=2.25l_\rho$, maximum plume height at a scale $X_{int}=2.85l_\rho$, and a neutral buoyancy level of the minimum-density plume fluid at a scale $X_{neut}=2.46l_\rho$.

The rescaled melting rate $\dot{m}/M_0U_u(l_\rho)=\mu u$ first increases with height, before decreasing to zero at the intrusion level $X=X_{int}$ (Figure 2f). In contrast, we note that the melt rate factor μ only varies slightly with height (Figure 2f). Hence the depth variation of melting rate is primarily controlled by variation in the plume velocity U and its impact on the parameterized turbulent heat transfer. The solutions here are derived for a vertically planar surface, and as such only describe a tendency for melting. However, such a nonuniform melting

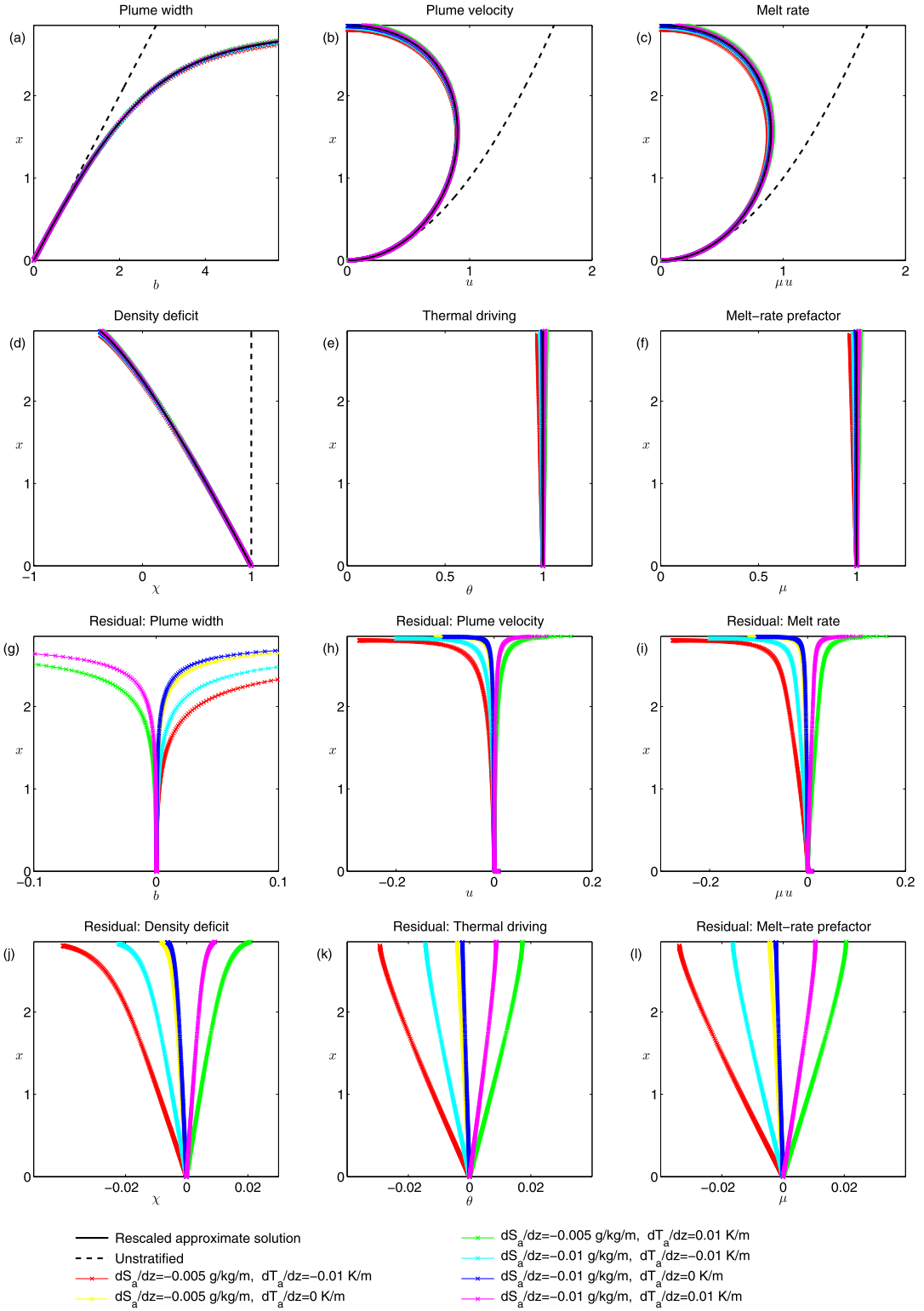

Figure 2. (a)–(f) Rescaled dimensionless plume profiles with rescaled depth x in a single layer of flow, for a range of ocean stratification conditions (colored lines) illustrated in the legend and $T_a = 2^\circ$C and $S_a = 35$ g/kg at the bottom of the layer at $Z = -500$ m. Black solid lines show the solution of the reduced model (45), while black-dashed curves show the corresponding solution for unstratified flow, which coincide with the black solid lines in Figures 2e and 2f. (a) Dimensionless plume width b, (b) dimensionless plume velocity u, (c) dimensionless melt rate μu, (d) dimensionless density deficit χ, (e) dimensionless thermal driving θ, and (f) melt-rate prefactor μ. Figures 2g–2l plot the corresponding residuals from each of plots (a)–(f), showing the difference between the full numerical solution minus the solution of the reduced model (45), for each of the stratification conditions indicated in the legend.

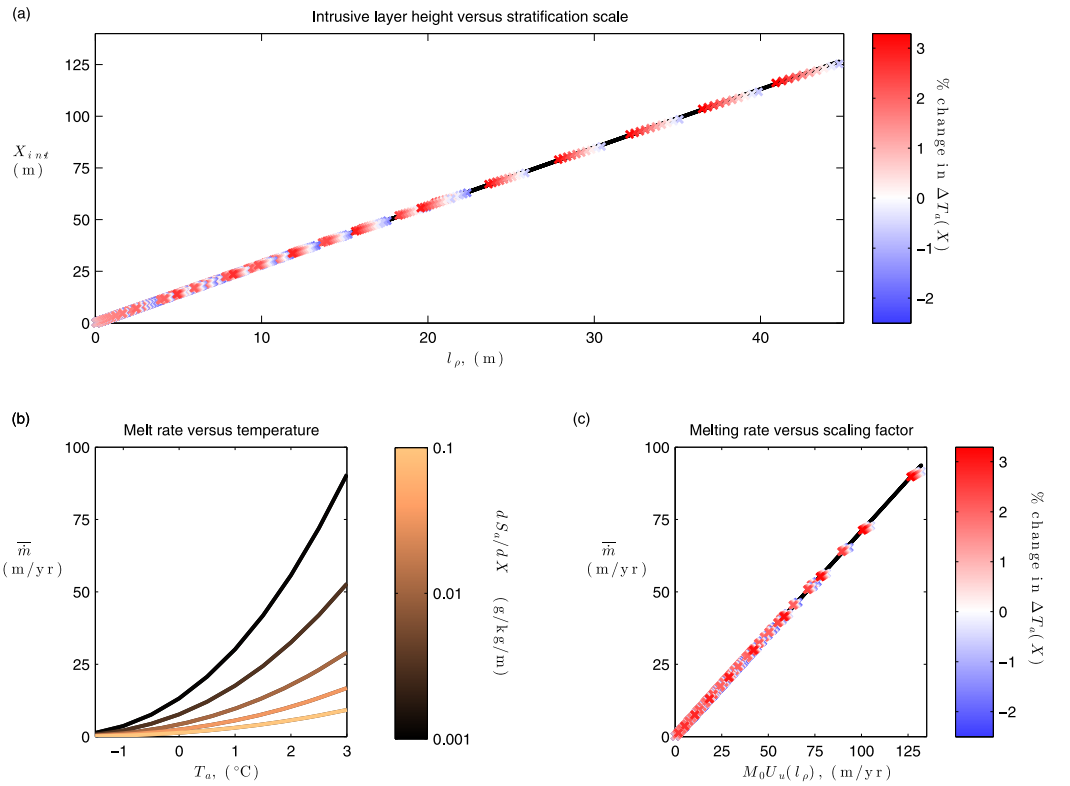

Figure 3. (a) Collapse of the distance X_{int} flowed before an intrusive layer forms as a function of the stratification scale l_ρ, for stratification conditions spanning the range (47). Solutions using the full model (18)–(25) are plotted using cross symbols, with the color scale indicating the %-change of $\Delta T_a(X)$ across the layer in each simulation (including nonzero λ). The data show only small deviation from a linear fit (underlying black line). (b) Depth-averaged melt rate $\overline{\dot{m}}$ predicted using the full plume model (18)–(25) as a function of ambient temperature T_a for a range of ambient salinity gradients dS_a/dX shown by the color scale, and $dT_a/dX=0$. (c) Collapse of $\overline{\dot{m}}$ versus the scaling $M_u(l_\rho)U_u(l_\rho)$ for the same range of parameter values and color scheme as in Figure 3a. The underlying black line shows a fitted linear trend. The initial ambient salinity $S_{a0}=35\,\mathrm{g\,kg^{-1}}$ and $T_s=-5^\circ\mathrm{C}$ in all plots.

pattern would promote notched undercutting if the flow structure is maintained as the ice face evolves by melting (discussed further in section 5).

To illustrate the effectiveness of the scalings across a broader range of ambient conditions, Figure 3a shows the variation of the dimensional intrusion height X_{int} determined from a numerical integration of the full unapproximated system (18)–(25), plotted against the stratification scale l_ρ, with the initial ambient temperature, $T_a(0)$, ambient temperature gradient dT_a/dZ, and ambient salinity gradient dS_a/dZ each varied over 10 values, yielding 10^3 configurations. To the extent that the values follow a linear relationship, there is a good collapse onto the expected scaling with a linear regression yielding

$$X_{int} \approx 2.83\, l_\rho. \tag{48}$$

This is close to the scaling $X_{int}=2.85\,l_\rho$ predicted by the reduced system (45) which neglects variations in ambient thermal driving over a layer height $(l_\rho d\Delta T_a/dX \ll \Delta T_{a0})$. There is some weak variability about this linear trend, consistent with the deviations in the ambient temperature over the depth of the layer, which are indicated by the color scale of the plotted symbols. Indeed, additional simulations (not shown here) reveal that there is a greater deviation from the linear relationship for conditions with far stronger thermal gradients than normally seen near Greenland fjords. However, over the range of stratifications considered here, the linear scaling (48) characterizes the intrusion height well. The predicted intrusive layer heights range from meters, to hundreds of meters as the strength of stratification varies over the range in the figure. Note that unstratified flow corresponds to the limit $l_\rho \to \infty$, so that an intrusion will not form before flow reaches either the ocean surface, or a level where the density stratification changes before an intrusive layer forms.

Figure 3c illustrates a corresponding collapse of predicted melt rates, averaged over the depth of an individual layer. Before rescaling, Figure 3b shows that the depth-averaged melt rate $\overline{\dot{m}}$ increases with ocean

temperature, but with significantly different magnitudes for different ambient density gradients. Figure 3c illustrates the collapse of depth-averaged melt rates against the scaling (38) over the broader range of stratification conditions considered in Figure 3a. The data lies close to a linear relationship

$$\overline{\dot{m}} \approx 0.71\,\Delta\rho_{i0}^{ef}\,\frac{M_0^2}{(E+M_0)}\left(\frac{2g}{4+3\mathrm{C_d}/(E+M_0)}\right)^{1/2}\left|\frac{\partial\rho_a}{\partial z}\right|^{-1/2}, \tag{49}$$

fitted by linear regression.

Similarly to the unstratified case, we can approximate (49) under the conditions (33), $M_0 \ll E$, and $\Delta T_{i0}^{ef} \approx -L/c_I$. For strong thermal driving with $\Delta T_{a0} \gg \Gamma(S_a - S_s)$, combining the above approximations with (35) and (49) yields

$$\overline{\dot{m}} \sim 0.71\left(\frac{c_p\Delta T_{a0}}{L}\right)^2 E\left(\frac{\mathrm{St}}{E+\mathrm{St}}\right)^2\Delta\rho_{i0}^{ef}\left(\frac{2g}{4+3\gamma}\right)^{1/2}\left|\frac{\partial\rho_a}{\partial z}\right|^{-1/2} \quad \text{for} \quad \Delta T_{a0} \gg \Gamma(S_a - S_s), \tag{50}$$

for the melting rate averaged over a flow layer (N.B. this scaling breaks down if the flow reaches the ocean surface before an intrusive layer forms). From (50), we see that the depth-averaged melting rate increases quadratically with thermal driving $\overline{\dot{m}} \propto (\Delta T_{a0})^2$, and decreases significantly as the ambient stratification increases. An increasing stratification restricts the layer height over which the flow develops, and thus limits the acceleration of the flow which impacts the velocity-dependent turbulent heat transfer. Hence stratified environments have lower flow speeds and melting rates than a plume in an unstratified environment with equivalent initial ambient temperature and salinity. However, there is a stronger dependence of melt rates on thermal driving for stratified flow than the corresponding unstratified flow, because of additional nonlinearity due to the development of layered flow. For larger thermal drivings, enhanced melting provides a greater buoyancy force, and thus the plume can accelerate a greater distance along slope before reaching a neutral buoyancy level. This allows stronger velocities to develop and further enhances turbulent heat transfer and melting for larger thermal drivings.

4.4. Solutions for Sloping Planar Ice Shelves

We next consider the flow development under a locally planar section of a sloping ice shelf base, inclined at an angle ϕ to the horizontal. For flows where the scaling estimates (44) hold, the reduced model (45) can still be applied under sloped surfaces but with the parameter $\gamma = \mathrm{C}_d/E_0\sin\phi$ dependent on the local slope angle. Figure 4a compares the dimensionless intrusion scale x_{int} (measured along slope) for solutions of the reduced system (45) shown by the blue solid line, to solutions of the full system (shaded circles) across a range of slope angles and ambient salinity stratifications, with constant ambient temperature $T_a = 0^\circ$C. Figure 4c shows a corresponding comparison for the dimensionless depth-averaged melt rate $\overline{\mu u}$. The reduced solutions show modest variation of the dimensionless intrusion depth (<35% variation) and dimensionless melt rate (<10% variation) with slope angle. The full solutions show slightly larger variability with slope angle, with the magnitude of deviation increasing as the density stratification weakens, or as the slope becomes shallower. Comparison to test simulations that set $\lambda = 0$ but are otherwise identical (shown by the star symbols) reveal that the majority of the discrepancy between the reduced and full model solutions is explained by variation of the freezing point temperature with pressure (and hence depth), which is neglected in the reduced solution. As illustrated on logarithmic scales in Figure 4b, the dimensional vertical layer spacing $Z_{int} = X_{int}\sin\phi$ increases significantly as the slope angle is reduced, which leads to the value of $\lambda I_\rho \sin\phi/\Delta T_u$ becoming significant. This partially violates (44) and gives rise to nonnegligible changes in the freezing temperature across the depth of the layer. With ambient temperature stratification, the increased layer depths also give rise to more significant variation of $\Delta T_a(Z)$ with depth (not shown here). Hence, the reduced scaling embodied in (38) and (45) is less accurate for sloping ice shelves in weak stratifications than it is for vertical ice faces. Nevertheless, the scaling still captures the correct order of magnitudes, particularly when the stratification is sufficiently strong.

The significant increase in layer depth Z_{int} as slope angle decreases (Figure 4b) is accompanied by nonmonotonic behavior of the depth-averaged melt rate $\overline{\dot{m}}$ (Figure 4d). The melt rate $\overline{\dot{m}}$ increases with slope angle for small angles, before decreasing as slope angle increases for larger angles. When $\Delta T_a \gg \Gamma(S_a - S_s)$, we can explain the observed scalings with slope angle by considering the behavior of the scales (38) for small and large slope angle. Setting $E = E_0\sin\phi$ and noting that $M_0 \ll E$, (35) yields

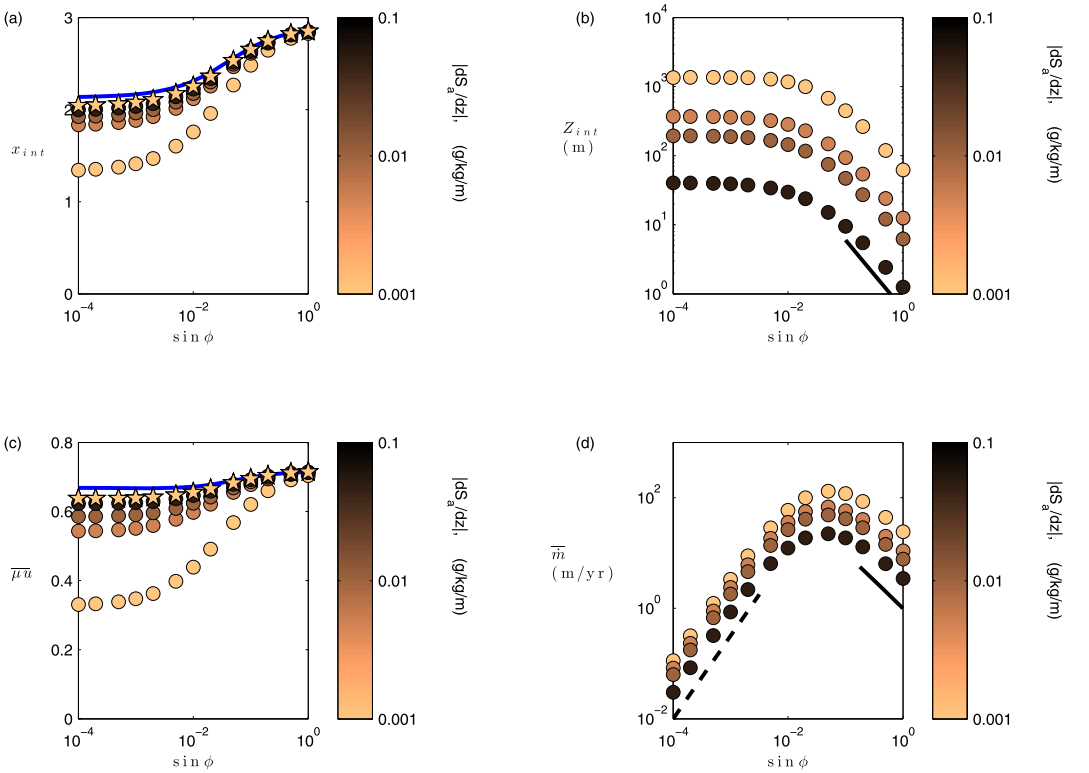

Figure 4. Simulated vertical intrusive layer spacing and depth-averaged melt rates for a range of ice shelf slopes sin ϕ and different ambient salinity stratification dS_a/dZ (shown by color of filled circles) with $T_a = 0^\circ$C constant in each layer, and $S_a = 35$ g/kg at the base of the layer. (a) Dimensionless layer scale x_{int}, (b) dimensional vertical layer height Z_{int}, (c) dimensionless depth averaged melt rate $\overline{\mu u}$, and (d) dimensional depth averaged melt rate $\overline{\dot{m}}$. In Figures 4a and 4c, blue curves illustrate results of the reduced model (45), while star symbols illustrate simulations of the full model but with $\lambda = 0$ artificially imposed to suppress pressure dependence of the melting point. In Figure 4b, the solid line indicates a scaling $Z_{int} \propto (\sin\phi)^{-1}$ while in Figure 4d the dashed line indicates a scaling $\overline{\dot{m}} \propto (\sin\phi)^{3/2}$ and solid line shows $\overline{\dot{m}} \propto (\sin\phi)^{-1}$.

$$M_0 \sim \frac{E_0 \sin\phi \,\mathrm{St}}{E_0 \sin\phi + \mathrm{St}} \frac{c_l \Delta T_{a0}}{L} \propto \begin{cases} (\sin\phi)^1 & \text{for} \quad E_0 \sin\phi \ll \mathrm{St}, \\ (\sin\phi)^0 & \text{for} \quad E_0 \sin\phi \gg \mathrm{St}. \end{cases} \tag{51}$$

The melting efficiency is limited by inefficient entrainment of heat for small slope angles, but inefficient turbulent transfer to the ice face when slopes and turbulent entrainment are larger. In the scales (38), the density deficit is controlled by the efficiency of melt input compared to entrainment of ambient water and this combines with the definition of the stratification scale (37) (noting again that $M_0 \ll E_0$) to yield the scaling

$$Z_{int} \propto l_\rho \sin\phi \sim \frac{M_0}{E_0 \sin\phi} \Delta\rho_{i0}^{ef} \left| \frac{\partial \rho_a}{\partial Z} \right|^{-1} \propto \begin{cases} (\sin\phi)^0 & \text{for} \quad E_0 \sin\phi \ll \mathrm{St}, \\ (\sin\phi)^{-1} & \text{for} \quad E_0 \sin\phi \gg \mathrm{St}, \end{cases} \tag{52}$$

where the final scaling limits have used (51) to substitute for M_0. This scaling behavior of layer depth with slope angle is consistent with the observed near-constant asymptote of Z_{int} for small ϕ, and comparable to the black line indicating a trend $Z_{int} \propto (\sin\phi)^{-1}$ in Figure 4b. Physically, as the slope angle is reduced from sin $\phi = 1$, the reduced entrainment of dense ambient fluid first allows a larger density deficit to be maintained, which allows the flow to traverse larger distances before reaching neutral buoyancy. For very small angles, the reduced entrainment also begins to throttle the melt rate efficiency and subsequently maintains a density deficit and intrusion depth that vary little with slope angle. We note that the numerical data in Figure 4b capture these trends despite being evaluated at $T_a = 0^\circ$C when the approximation of the ambient thermal driving $\Delta T_a \gg \Gamma(S_a - S_s)$ is not strictly valid, which suggests the scaling with slope angle may have broad utility for lower temperatures.

The variation in stratification scale in (52) also contributes to the dimensional melt-rate scaling with slope angle. Using the approximation $M_0 \ll E$ in (38), we have

$$\overline{\dot{m}} \sim \mu u M_0 \left(\frac{2E_0 \sin\phi}{3C_d + 4E_0 \sin\phi}\right)^{1/2} \left(\frac{\Delta\rho_u}{\rho_l} g l_\rho \sin\phi\right)^{1/2} \propto \begin{cases} (\sin\phi)^{3/2} & \text{for } E_0 \sin\phi \ll \mathrm{St},\ C_d \\ (\sin\phi)^{-1} & \text{for } E_0 \sin\phi \gg \mathrm{St}, C_d, \end{cases} \tag{53}$$

where we have applied the scalings (51) and (52), substituted for $\Delta\rho_u$ using (38), and neglected the modest dependence of μu on ϕ at leading order. The trend in simulated melt rate yields good comparison with the scalings $\dot{m} \propto (\sin\phi)^{3/2}$ and $\dot{m} \propto (\sin\phi)^{-1}$, indicated by the trends of black lines for small and large $\sin\phi$ on the log-scales in Figure 4d. Physically, the increase in melting rate with slope angle for small slopes is controlled by the impact of increased entrainment on both the heat flux for melting through (51), and by increasing the plume width. To explain the latter effect, we note that at small slope angles the dominant momentum balance is between buoyancy and drag [cf., *Lane-Serff*, 1995]. Hence, the increase in plume width reduces the effectiveness of the drag per unit mass of plume fluid, allowing larger velocities to develop which in turn enhance melting. In the second limit for larger slope angles, the momentum balance is between inertial acceleration and buoyancy, with the increase in entrainment and plume width with slope angle leading to compensating changes to inertial and buoyancy forces. The reduction in melt rate as slope angle increases is then driven by the reduction in the density deficit and layer depth in (52), which limit the acceleration of the plume before it reaches the neutral buoyancy level. This limits the velocity, turbulent heat transport, and melting. We note also that the above solutions under sloping ice shelves break down when $g\Delta\rho D\cos\phi/U^2 > 1$, the flow speed is subcritical with respect to gravity waves, and the neglect of alongslope gradients in hydrostatic pressure is no longer justified. In particular, this condition will apply very close to the intrusion level, where $U \to 0$.

4.5. Geophysical Case Studies

We illustrate the application of our theoretical results to two cases studies motivated by previous ocean observations near Hellheim glacier terminus in Sermelik fjord, Greenland [*Straneo et al*., 2012] and Erebus ice tongue, Antarctica [*Jacobs et al*., 1981].

Figure 5a illustrates piecewise-linear ocean temperature and salinity stratifications, motivated by observations of oceanographic conditions in Sermelik fjord in winter [*Straneo et al*., 2012], when we expect subglacial discharge to be low and the theory here to be more relevant.

We compare numerical solutions of the full plume model (18)–(25) (red curves) with solutions of the reduced model (45) (black curves), using the ocean stratification from each of the shaded regions (I) and (II) in Figure 5a. To facilitate a direct comparison of layer properties over a region of uniform stratification, both models are initiated with matching initial conditions at the base of each of the individual layers at depths $Z = -220$ m and $Z = -335$m. When started with the same initial conditions, the full and reduced models yield very similar behavior, with a repeating series of layered intrusions (initiated where D diverges in Figure 5b). Note that this pattern shows qualitative similarities with previous numerical results for ice shelf melting [*Jenkins*, 1993]. The layered melting pattern (Figure 5c) would have a tendency to generate notches and localized undercutting in an initially planar interface. Layer depths of order $5-10$ m are observed in the strongly stratified region (I), rising to $O(40\,\mathrm{m})$ in the weaker stratification in region (II). The layer scaling and peak melt rates in each layer both reduce as depth reduces, even with a constant ambient density gradient. The reduction of ambient temperature and salinity as we move up into a new layer reduces the thermal driving, causing a reduction in melt rate and thus also in the driving density difference, which reduces the layer scaling (48). A similar pattern of layered flow is found in the surface layer $-Z < 135$ m with an intermediate value of the layer height (not shown) lying between the illustrated cases with stronger and weaker stratification.). For the deepest region $335\,\mathrm{m} < -Z < 600\,\mathrm{m}$, the stratification is sufficiently weak that the flow rises through the full depth of the layer without intruding (not shown here), with the full and reduced models in reasonable agreement. When initiated at the same depth in a constant temperature and salinity gradient, the reduced solution slightly overestimates the layer depths compared to the full solution, with the discrepancy accumulating over multiple layers. The correspondence is reasonable for most practical purposes, unless $O(\mathrm{m})$ scale accuracy is demanded for the spatial distribution of melt. We note that a full parameterization of melt over the entire ice face requires a careful treatment of flow across the changes in ambient density gradient (discussed further in section 5.4).

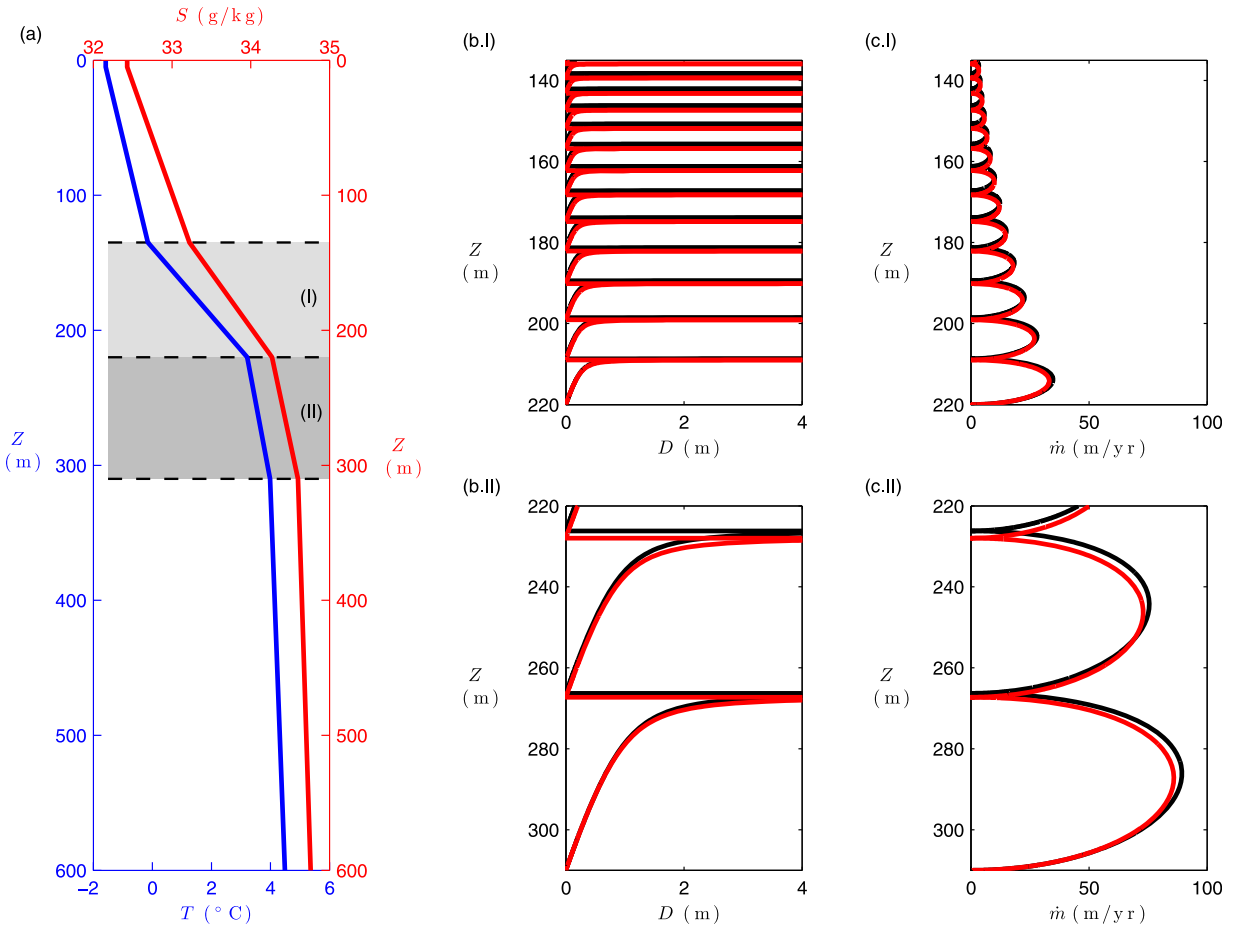

Figure 5. Case study for melting of Hellheim glacier in Sermelik fjord in winter. (a) Piecewise-linear approximation to variation of ocean Temperature (blue curve, lower scale) and ocean salinity (red curve, upper scale) with depth – Z. Variation with depth of modeled plume width (plots b.I and b.II) and melt rate (plots c.I and c.II) are illustrated for integrations started at the bottom of each layer marked by the shaded regions (I) and (II) in Figure 5a. In columns (b) and (c) red curves correspond to solutions of the full plume model (18)–(25) while black curves show solutions of the reduced model (45).

We also compare to oceanographic observations of layered ocean temperature and salinity profiles in the vicinity of Erebus ice tongue. *Jacobs et al.* [1981] observed ambient ocean temperature and salinity properties consistent with alternating steps of stratified density gradient, and well-mixed layers. While a range of mechanisms could contribute to the formation of such steps, one possibility is that layered outflows from rising meltwater plumes may punctuate the density stratification. The detailed interaction with the stratification would depend on the extent of vertical rebound and mixing as the intrusion flows away from the ice face, but we might expect the scales of these layers to inherit the characteristic length scale for the layered intruding plumes. *Jacobs et al.* [1981] observed layer thicknesses for a selection of depths, which were predominantly larger than the layer thickness predicted using the scaling of *Huppert and Turner* [1980] given later in (54), based on quasi-laminar laboratory experiments. In Table 3, we compare the observed layer thicknesses and scalings (54) as reported by *Jacobs et al.* [1981] (their Table 1), with predictions from the present turbulent plume theory for a range of assumptions regarding the ice shelf basal slope.

We restrict attention to depths $50\,\mathrm{m} \leq -Z \leq 250\,\mathrm{m}$ that are above the grounding line of the ice shelf (as illustrated in Figure 3 of *Jacobs et al.* [1981]) and neglect the layer at $Z = 0$ which is likely to have been influenced by the surface mixed layer. Following the approach in *Jacobs et al.* [1981], we assume that the flow responds to the mean background stratification rather than individual layers, and construct a piecewise linear stratification over the two intervals $50\,\mathrm{m} \leq -Z \leq 100\,\mathrm{m}$ and $100\,\mathrm{m} \leq -Z \leq 250\,\mathrm{m}$ based on the observed significant break in the stratification. For the surface layer in the region $20\,\mathrm{m} \leq -Z \leq 50\,\mathrm{m}$, we extrapolate dS_a/dZ from the underlying layer, but impose $dT_a/dZ = 0$ (motivated

Table 3. Predicted Layer Thicknesses h and Depth-Averaged Melt Rates $\overline{\overline{m}}$ for Conditions Relevant to Erebus Ice Tongue, Antarctica[a]

Scaling				*Observed*	*HT*	*Full*	*Reduced*	*Full*	*Reduced*
$-Z$ (m)	$T_a(Z)$ (°C)	$S_a(Z)$ (g kg^{-1})	$\sin\phi$	h (m)	h (m)	h (m)	h (m)	$\overline{\overline{m}}$ (m yr^{-1})	$\overline{\overline{m}}$ (m yr^{-1})
50	−1.23	34.41	1	17	14	5.5	5.5	0.64	0.64
			0.0274			50.0	104.4	4.25	4.85
100	−1.35	34.52	0.3106	27	13	14.2	14.2	1.39	1.38
			1			4.7	4.7	0.50	0.49
			0.0274			92.4	88.5	4.05	3.75
150	−1.53	34.59	0.1319	29	11	39.5	37.5	2.06	1.89
			0.048			90.6	79.9	3.48	2.82
			1			5.9	5.9	0.37	0.37
			0.0274			136.2	111.6	3.94	2.84
200	−1.72	34.65	0.1319	31	7	27.6	26.2	1.00	0.92
			0.0484			63.1	55.7	1.70	1.38
			1			4.1	4.1	0.18	0.18
			0.0274			95.6	78.4	1.94	1.40
250	−1.90	34.71	0.0594	34	4	31.0	27.9	0.52	0.44
			1			2.4	2.3	0.06	0.06
			0.0274			55.3	45.4	0.65	0.47

[a]Observed ambient temperatures T_a and salinities S_a at a variety of depths $-Z$ [*Jacobs et al*., 1981] are used to construct a stratification as described in the main text. Observed intrusion thicknesses h are compared with model predictions using the slope-independent theory of Huppert & Turner (HT), and the full model (18)–(25) and reduced model (45) for a range of slopes $\sin\phi$ corresponding to local estimates of ice shelf basal slope at each depth, a vertical ice face ($\sin\phi=1$), and the mean basal slope of the ice shelf ($\sin\phi=0.0274$). We also estimate depth-averaged melt rates $\overline{\overline{m}}$ for the full and reduced models.

by the stratification in Figure 3 of *Jacobs et al*. [1981]). The pointwise measurements of ice shelf thickness illustrated by *Jacobs et al*. [1981] are suggestive of complex basal topography, with nonmonotonic variations of thickness along the shelf and some uncertainties over the slope. This complicates the application of a single plume model integration along the entire shelf, and so we instead probe the uncertainty by calculating the predicted thickness of a new layer of flow initiated at each sample depth, making a range of assumptions about the slope. At each depth, we estimate the positive values of the local ice shelf slope facing toward the open ocean (from the radar data plotted in Figure 3 of *Jacobs et al*. [1981]). For some depths, this produces two estimates of slope, due to the nonmonotonic variation of ice thickness. To illustrate the sensitivity to assumed slope, we also list results assuming a locally vertical ice face, and using the mean slope $\sin\phi=0.0274$ of the full sloping ice shelf base. For the near surface layer starting at $Z=-50$ m, we assume a vertical ice cliff.

For the deepest layers over $150\,\text{m} \leq -Z \leq 250\,\text{m}$, at least one of the local ice shelf slopes predicts a layer spacing within the range 28−40 m, in decent order-of-magnitude agreement with the observed layer depths in the range 29−34 m. The scaling of *Huppert and Turner* [1980] tends to underestimate layer thicknesses over this depth range. For the near surface layers at $Z=-50$ m and $Z=-100$ m, the plume model tends to underpredict layer thicknesses by a factor of 2–3, yielding a similar or lower estimate than the scaling of *Huppert and Turner* [1980]. However, most notable is the significant dependence on the assumed ice shelf slope, with layer thicknesses varying by factors of 2−2.5 where multiple values of local slope are possible. (Clearly predicted layer thicknesses greater than 50 m might experience changes in local slope and cause the approximation here to break down, but the estimates do serve the purpose of illustrating significant sensitivity to slope). Furthermore, predicted layer thicknesses vary by a factor of order 20 between using a uniform mean slope for the entire shelf, or assuming that the observed layers originate from locally vertical regions of roughness on the ice shelf base. In light of observations of complex ice shelf topography [*Dutrieux et al*., 2014], this highlights the potential significance of accurately characterizing basal slope in order to predict ice shelf melting.

The predicted values of depth-averaged melt rate in each layer are broadly commensurate with the observational estimate of 1.4m/year averaged over the whole ice shelf face [*Jacobs et al*., 1981]. A closer comparison is not justified without a more detailed treatment of ice-shelf basal topography. In summary, the reasonable order-of-magnitude agreement without fitting parameters is an encouraging result, but this slightly speculative comparison should be treated cautiously in light of the potential uncertainties in ice shelf geometry, model parameters, and alternative forcing mechanisms that could also be relevant. The

results do however indicate the range of scales that might be expected to occur in such environmental settings.

5. Discussion

5.1. Comparison to Previous Laboratory Experiments

The melting of initially planar, vertical ice blocks in a salt-stratified fluid has been considered in previous laboratory experiments [*Huppert and Turner*, 1978, 1980] and we highlight key similarities and differences with our model of turbulent geophysical scale flow. Huppert and Turner characterize the vigor of turbulent convection using a dimensionless Grashof number $\mathrm{Gr}=g\Delta\rho L^3/\rho_0\nu^2$, where L is the characteristic along flow distance, ν is the kinematic viscosity, and the characteristic density difference can be approximated by $\Delta\rho \approx \rho_0\beta(S_a-S_s)$ for dominant compositional convection. For laboratory experiments with $\mathrm{Gr} < 10^{10}$, Huppert and Turner observed layered outflows, but with a subtly different mechanism to that considered here. The interpretation of the observed flow features is consistent with double diffusive behavior due to different diffusivities of heat and salt, with a narrow and fresh compositional boundary layer nested in a broad and cold thermal boundary layer at ambient salinity. The cold outer boundary layer has higher density than the ambient, and sinks before intruding into the ambient at neutral density. This flow gives rise to a repeating series of layers with spacing

$$h=(0.66\pm 0.06)[\rho(T_m,S_a)-\rho(T_a,S_a)]\left|\frac{\partial\rho_a}{\partial Z}\right|^{-1}, \tag{54}$$

where $\rho=\rho(T,S)$. The rising fresh compositional boundary layer was reported to flow into the ambient over the course of 2–3 layers. The scaling (54) exhibits some similarities with our predicted layer spacing for a turbulent plume, scaling proportional to a characteristic density difference and inversely with ambient density gradient. The significant difference is that the turbulent plume model assumes a well-mixed plume core yielding a prediction (48) based on the salinity-dependent density difference between the ambient and the upward flowing plume. In contrast, the laboratory-scale correlation assumes a separation of thermal and solutal boundary layer variation, with (54) based on the density difference between the ambient and a downward flowing cold thermal boundary layer.

So are the conventional plume theories [e.g., *Jenkins*, 2011] capturing the right dynamics? Glacier terminus and ice shelf melting correspond to far larger Grashof numbers than for the laboratory experiments, with $\mathrm{Gr} \sim 10^{20}$ for a 1000 m deep glacier terminus melting in water of $S_a=35$ g/kg. Previous theories and laboratory experiments for related heat transfer problems indicate that we might expect dynamical flow transitions to occur over this range of Grashof numbers, between quasi-laminar flow on laboratory scales, and vigorous turbulence on geophysical scales [see *Wells and Worster*, 2008, for a discussion]. It remains to be proven whether the self-similar plume theory for unidirectional flow is sufficient, or a revised model is required accounting for solutal and thermal boundary layers within the core of the turbulent plume. If suitable observations were available of boundary-layer dynamics at ice faces, this distinction could be inferred from the presence or absence of a bidirectional boundary layer flow with fresh upwelling near to the ice face and cold downwelling at a greater distance from the ice face.

5.2. Melting Rate Dependencies on Temperature and Shelf Slope

For our analysis of meltwater convection with negligible subglacial discharge, we have identified two distinct scalings for melting rates for unstratified and linearly stratified flow, given by (36) and (50), respectively, in the limit of large thermal driving. These results can be compared with a range of temperature dependencies for alternative settings where different processes dominate. The nature of the heat transfer parameterization (12) and Stefan condition (7) imply that melt rates depend on the product of characteristic temperature and velocity scales. Thus we expect an approximately linear dependence of melt rate on thermal driving $\overline{\dot{m}} \propto \Delta T_a$ in settings where the dominant velocity is independent of temperature, such as tidally driven flows [e.g., *Holland*, 2008] or meltwater plumes dominated by an imposed strong subglacial discharge [e.g., *Jenkins*, 2011; *Sciascia et al*., 2013; *Xu et al*., 2013]. When the ocean temperature provides a feedback on the velocity scale, we expect a more complex nonlinear dependence of melting on thermal driving (see discussion in *Holland et al*. [2008b]; *Little et al*. [2009], for shelf settings). *Holland et al*. [2008b] find a quadratic dependence $\overline{\dot{m}} \propto \Delta T_a^2$ when the supply of meltwater controls the strength of a geostrophic

flow under an ice shelf. For large thermal driving, our model of convection driven by interfacial melt predicts $\overline{\dot{m}} \propto \Delta T_a^{3/2}$ for flow in an unstratified ocean, and $\overline{\dot{m}} \propto \Delta T_a^2$ for flow in a linearly stratified ocean, with more complex dependencies for very small ΔT_a that cannot be characterized as a power law in ΔT_a. We note that in a limit of weak subglacial discharge, *Xu et al*. [2013] approximated $\overline{\dot{m}} \propto \Delta T_a^{1.6}$ using an ocean circulation model for flow along a vertical calving face in a variable stratification combining an unstratified segment at depth with variable near-surface stratification. This scaling lies between the two limits predicted here for stratified and unstratified flow.

The heat transfer parameterization (12) can also result in slope-dependent melting rates via the impact of slope-dependent entrainment on U and ΔT, along with the slope-dependent buoyancy force acting to accelerate the flow. For convection driven by interfacial melt in a stratified fluid, we find complex nonmonotonic scaling of the depth-averaged melt rate with ice shelf slope in (53), with $\overline{\dot{m}} \propto (\sin\phi)^{3/2}$ for small slopes, and $\overline{\dot{m}} \propto (\sin\phi)^{-1}$ for larger slopes. For convection driven by strong subglacial discharge, the scalings in *Jenkins* [2011] yield a similar separation of regimes but with different exponents, with $\overline{\dot{m}} \propto (\sin\phi)^{2/3}$ for small slopes, and $\overline{\dot{m}} \propto (\sin\phi)^0$ asymptoting to a slope-independent limit for large slope angles. This diversity of scalings, across only two of the possible mechanisms for driving flow, highlights that the variation of melting rate with slope depends sensitively on the details of the configuration at hand. This echoes the conclusion of *Little et al*. [2009] who found complex changes to the dependence of melt rate as the ice shelf morphology varied in an ocean circulation model. Note also that when melting is strong, the actual slope of an ice shelf will be determined in part by the melting rate itself [e.g., *Sergienko et al*., 2013].

5.3. Sensitivity, Limits of Applicability, and Uncertainties

The results thus far rely on several assumptions or specified parameters, which we revisit below and discuss potential extensions.

5.3.1. Sensitivity to Initial Conditions

When initiating a new layer, we assume that the flow quickly establishes a self-similar state immediately above the intrusion by mixing with the ambient fluid. Modest variations to the initial fluxes of mass, momentum, and heat typically result in the fluxes rapidly approach the attracting state after a brief initial transient (not shown here) as is common in plume models dominated by buoyancy fluxes [cf., *Dallaston et al*., 2015]. Of greater significance is the input of subglacial discharge at the grounding line, which impacts the buoyancy flux in the first layer and can dominate if discharge is strong [*Jenkins*, 2011]. We expect subglacial discharge to dominate the buoyancy force when the subglacial volume flux Q_{sg} is larger than the input from melting of the submerged ice face, but will be less significant beyond a scale Z_{sg} determined by

$$Q_{sg} \ll \int_{\text{plume}} \int_H^{Z_{sg}} \dot{m}\, dZ\, dY, \tag{55}$$

where the Y-integral corresponds to averaging over the width of the subglacially dominated plume. The precise value obtained depends on the strength and geometry of the assumed discharge and how it develops along slope.

5.3.2. Sensitivity to Parameters

The approximate analytical results (50)–(53) and their application in the reduced scalings provide an indication of sensitivity to model parameter uncertainty, which depends on ice-shelf slope. For the limit of strong thermal driving, the parameter sensitivity for the layer scale is carried through $\Delta\rho_u \sim \Delta\rho_i^{ef} M_0/E$ with M_0 given by (35), while the melting rate sensitivity is illustrated by (50). In the steep slope limit with $E_0 \sin\phi \gg \text{St}, \text{C}_d$, we recover a leading-order scaling $\Delta\rho_u \propto \text{St}/E$ so that layer depths will vary almost proportionally to changes in St and inversely proportionally to changes in E, but with only weak dependence on the drag coefficient C_d. The depth-averaged melt rate scaling (50) has dominant parameter dependence $\overline{\dot{m}} \propto \text{St}^2/E$ for steep slopes with $E_0 \sin\phi \gg \text{St}, \text{C}_d$. Thus the melt rate depends strongly on St and E, but only weakly on C_d. In the shallow slope limit with $E_0 \sin\phi \ll \text{St}$ and $E_0 \sin\phi \ll \text{C}_d$, we recover $\Delta\rho_u$ and Z_{int} being approximately independent of E, St and C_d at leading order, with weak higher-order corrections (this also ties in with the asymptotic limits leading to slope independence in Figure 4b). Approximating (50) with $\gamma = C_d/E_0 \sin\phi \gg 1$, the melt rate now has leading-order parameter dependence $\overline{\dot{m}} \propto E^{3/2}/\text{C}_d^{1/2}$ showing strong dependence on the entrainment coefficient and drag coefficient, but weaker dependence on the heat transfer coefficient.

For weaker thermal driving, where salt transport becomes significant, the structure of the melt rate factor (25) suggests that the sensitivity to the salt transfer coefficient St_m will have similar prominence to sensitivity to the heat transfer coefficient St. This strong parameter sensitivity has both pros and cons. While the parameter values remain uncertain, such uncertainty propagates into the magnitude of flow scales and flow structure. However, strong sensitivity allows the admissible range of parameter values to be more easily constrained via comparison to observations (with the Erebus case study in section 4.5 providing an encouraging initial investigation).

5.3.3. Evolution of Ice Face Geometry

The calculations have assumed a locally planar ice face, but predicted tendencies for melting rates that vary with depth that would slowly modify the ice geometry over time and eventually depart from the planar theory. If the predicted melt patterns were to remain fixed as an initially vertical ice face evolved, this would lead to the formation of regions of upward facing ice surface. Such adverse slopes no longer confine the buoyant meltwater adjacent to the ice face, and could allow flow separation with the meltwater plume detaching from the ice and the model breaking down. This effect may initially be countered by Bernoulli suction with the pressure in the fast-moving plume being of order $\Delta p \sim \rho_l U^2$ lower than in the ambient ocean. The issue is also less likely to arise for inclined ice faces that confine the buoyant meltwater from above.

Modifications to the ice geometry would also impact the glaciological stresses in the ice sheet or ice shelf. For near vertical ice cliffs, uneven melting could lead to undercutting, which may promote calving. The melting rates predicted here of course occur in tandem with intermittent background calving events which strongly modify the ice geometry. It is plausible to envisage a scenario where each intermittent calving event exposes a new ice face to the action of melting, and removes memory of the earlier melting pattern. An assessment of this scenario requires a more detailed treatment of ice stresses and deformation, along with calving forced by melt-induced changes to the ice geometry [cf., *O'Leary and Christoffersen*, 2013].

A third geometrical impact is the effect of horizontal curvature of the ice face. One might reasonably justify the application of the theory to a local orthogonal curvilinear coordinate system-oriented parallel and perpendicular to the ice face, provided that the plume width is narrow compared with the radius of curvature of the ice face (so that neighboring regions of plume do not strongly interact).

In summary, the present results can be viewed as providing insight into melting tendencies for locally planar regions of ice face, but some uncertainties remain over the interaction of layered flows with an evolving ice shelf geometry, particularly for near-vertical ice faces. A detailed treatment of the feedbacks on melting of such an evolving ice geometry may be an interesting topic for future work.

5.3.4. Fate of Layered Outflows

The model predicts that the inertia of the rising meltwater causes the flow to overshoot its neutral density level before intruding into the ambient. The resulting outflow in each layer is thus initially negatively buoyant compared to the background stratification, which would cause the intruding water mass to sink towards its neutral density level as it flows away from the ice face. At the same time, the plume waters are statically unstable with respect to the immediately underlying ambient fluid, and we thus expect convective mixing with the underlying fluid in addition to shear-driven mixing. The balance of sinking of the core of the current to mixing with underlying fluid will control the depth, temperature, and salinity characteristics of the outflow into the fjord. While the details of this balance remain unquantified, we would initially expect such outflows to lie in a region of temperature-salinity space spanned by mixing lines between the final plume density at each intrusion, and the ambient temperature and salinity conditions between the intrusion height and the neutral density level. This conceptual picture is consistent with work on axisymmetric buoyant plumes in stratified ambients [*Morton et al*., 1956] and the rebound of wall-bounded density currents [*Baines*, 2005], which have shown that intrusive outflows occur between the maximum rise height and the neutral buoyancy level predicted by the plume theory. In profiles of $T(Z)$ and $S(Z)$ downstream of the ice face, one might expect to see the background stratification punctuated by layers of contrasting temperature and salinity gradients corresponding to the outflow and its mixing with the environment. These outflow mechanisms also have the potential to modify the ambient stratification over time, as freshwater from the glacial melt is vertically redistributed through the ambient waters. Whether the evolving stratification provides a strong feedback on melting will depend on the balance of other mixing processes and transport that control the renewal of fjord waters. For example, this flow structure could be modified by the presence

of strong externally forced shear flows driven by winds or tides, in settings where such flows dominate compared to buoyancy-driven flow described here.

5.3.5. Detrainment

Our model has assumed that there is continuous entrainment along the length of the current, so that detrainment only occurs via the outflow discussed in section 5.3.4. Hence we have implicitly neglected any continuous detrainment of fluid along the length of the flow. The significance and location of detrainment from buoyant flows in stratified fluids is currently a topic of debate. Laboratory experiments of dense overflows and plumes show that continuous detrainment can be significant in some settings [e.g., *Baines*, 2005; *Gladstone and Woods*, 2014; *Hogg*, 2014; *Hogg et al*., 2016], but is less significant in others [e.g., *Morton et al*., 1956; *Baines*, 2005] where entraining plume models make successful predictions of maximum plume rise heights. *Baines* [2005] described detrainment of fluid in a dense overflow linked to Holmboe instabilities shedding fluid from the plume. However, experiments on stratified shear flow in channels suggest that Holmboe instabilities are suppressed at sufficiently large Reynolds number in favor of vigorous turbulent mixing [*Meyer and Linden*, 2014], likely linked to Kelvin-Helmholtz instability. There is currently a lack of compelling observational evidence for whether or not continuous detrainment is significant in geophysical scale flows, where Reynolds numbers are typically larger than on the laboratory scale.

In the supporting information section S2, we consider a simple mixing length argument, building on a conceptual model of peeling detrainment by *Hogg* [2014] and *Hogg et al*. [2016], in an attempt to rationalize whether detrainment would be significant for the present meltwater flows. The scaling argument suggests that detrainment may be less significant over a majority of the flow, until the flow approaches the neutral density level. Thereafter, detrainment may become significant compared to entrainment by shear-driven turbulence. For flows under sloping ice shelves, the plume becomes negatively buoyant and hence statically unstable beyond the neutral density level. If this negative buoyancy overcomes any tendency for shear-driven entrainment, then there is a clear mechanism for detrainment whilst the flow decelerates and loses its alongslope inertia. Thus, continuous detrainment may be significant over the region between the neutral density level and the maximum rise height, and the predicted flow structure should be treated with caution over this region (which typically comprises up to 20% of the predicted flow length). Such detrainment may contribute to and interact with the complex dynamics of the outflow as it rebounds toward the neutral density level, and could be important for understanding the eventual fate of meltwater flow away from the ice. Hence building a more detailed understanding of the detrainment process provides an interesting topic for future work.

5.4. Basis for a Parameterization

The scaling laws for unstratified and stratified flow offer the potential to be developed into parameterizations of melting in ocean models for regions of the ice face that are not strongly influenced by subglacial discharge. This would complement existing parameterizations of localized melt from subglacially dominated plumes [*Cowton et al*., 2015], by providing a dynamically determined background melting rate that operates over large areas of an ice face between the subglacially fed plumes. Nonlinear stratifications could be approximated via a piecewise-linear discretization of the ambient stratification derived at each time step of the ocean model, and then the reduced solution could be used to parameterise meltwater outflow with depth across each layer. Alternatively, one could use the scaling laws to construct an ice shelf basal melting parameterization for ice-sheet models, given an assumed ocean stratification. For greatest fidelity, such a parameterization would combine results from the present strongly stratified limit to alternative limits dominated by subglacial discharge [*Jenkins*, 2011; *Cowton et al*., 2015] and change of the pressure-dependent melting point with depth [*Gudmundsson and Jenkins*, 2015] which can induce supercooling, frazil ice formation, and basal accumulation [*Jenkins and Bombosch*, 1995]. The coriolis force may also become significant for large-scale flow under shallow-sloping shelves. The results presented here for shelves might reasonably apply on scales smaller than the Rossby deformation radius, or when the flow is geometrically confined by ice topography or bathymmetry. We hope that such a parameterization would provide a useful tool to assess some of the feedbacks of evolving ice geometry and ocean stratification on plume flow, as discussed in section 5.3.

6. Summary and Conclusions

We have considered the melting of locally planar ice faces into a stratified fluid, relevant to both near vertical glacier termini and sloping ice shelf bases in cases where the flow can be treated as effectively one-

dimensional along a flow line. Focussing on flows with negligible subglacial discharge, a plume model predicts that layered flows develop when there is a strong linear stratification dominated by salinity variations. Buoyant fresh meltwater mixes with ambient fluid as it rises, and the mixture can eventually reach a neutral density level with subsequent deceleration of the flow and intrusion of plume waters into the ambient. Repeating layered flows form if the ocean is sufficiently deep compared to the layer depth; otherwise the layer will outcrop and flow out at the free surface. Starting from an initially planar surface, the melting pattern predicts a tendency for notched melting and localised undercutting, although further work is required to fully ascertain the feedbacks between the meltwater flow and significant changes in slope.

A key result of the analysis was determining the dominant scales (38) and reduced solution (45) for the flow. These scales depend on a characteristic stratification length scale, which corresponds to the height a parcel of initial plume mixture would need to rise through the background stratification to attain neutral buoyancy. These scales lead to a reduced model for the flow, using common universal shape factors to capture the leading-order dynamics across a range of ocean conditions for which the validity conditions (44) hold. Most notably, the validity conditions require that the ambient freezing temperature does not vary too much across a layer. The reduced model yields good comparison to full numerical solutions for vertical ice faces under the stratification conditions considered, that were motivated by Greenland fjords. Pressure-dependent variations of the freezing temperature with depth become more significant for ice shelves with shallow basal slopes or in weak stratifications. The reduced scaling still captures the order of magnitude of intrusion scales and melt rates in these shelf settings, but might be quantitatively improved by a theory that accounts for corrections due to variation of the freezing temperature with depth. The scalings predict that the vertical spacing between intrusive layers decreases as either the stratification strengthens, or the thermal driving weakens and reduces melting. Increasing the stratification reduces the depth-averaged melting rate, by reducing the vertical scale over which the strength of flow can develop. We have also identified nonlinear variations of the melting rate with ocean temperature and ice shelf slope. A comparison of model predictions to estimated melt rate and thickness of layers in the stratification near Erebus ice tongue yields encouraging results, although the model predictions are very sensitive to uncertainties in the local ice shelf slope. Notably, very different predictions are obtained using a mean slope, versus local segments with piecewise linear slope, suggesting that in some circumstances a detailed knowledge of the ice geometry may be necessary for high fidelity predictions.

There is potential for the scalings derived here to be used as a parameterization of glacial melt, in regions where a near-uniform salinity gradient persists over several layer thicknesses. As in the comparison to the data for Erebus ice tongue, pointwise comparisons can be used for order of magnitude estimates. A full parameterization of detailed melting patterns over an entire ice face would need to deal with changes of slope and stratification with depth, and integration of results for the present limit of strong stratification and weak subglacial discharge with work in different regimes where there is strong subglacial discharge [*Jenkins*, 2011] or significant variation of the depth-dependent freezing points. The results would also need to be extended to account for coriolis forces in cases with large-scale two-dimensional circulation under ice shelves, over length scales larger than the deformation radius. We hope that the scalings developed here provide a useful step toward such a goal.

Appendix A: Melt Rate Approximation

For unstratified flow, the melt rate can be conveniently approximated by making a few asymptotic simplifications. First, we note that (29) and (30) combine with (26) to show that

$$\Gamma(S-S_s)=\frac{E}{E+M_0}\Gamma(S_{a0}-S_s), \tag{A1}$$

for the unstratified similarity solution (without approximation). We now note that typically $c_s[T_s-T_L(S_s)]/L \ll 1$ and $c_s[T_s-T_L(S)]/L \ll 1$ so that the coefficients (24) are approximated by

$$a \approx 1, \quad b \approx \mathrm{St_m}-\mathrm{St}\frac{c_l[\Delta T-\Gamma(S-S_s)]}{L}, \quad c \approx -\mathrm{St_m}\mathrm{St}\frac{c_l\Delta T}{L}.$$

Hence, (A1) and (29) can be used to show that the melt rate M_0 satisfies

$$M_0^2\left[1-\frac{\mathrm{St}}{(E+M_0)}\frac{c_l\Delta T_{i0}^{ef}}{L}\right]-\frac{\mathrm{St_m St}\,E}{(E+M_0)}\frac{c_l\Delta T_{a0}}{L}+\ldots$$

$$+M_0\left\{\mathrm{St_m}\left[1-\frac{\mathrm{St}}{(E+M_0)}\frac{c_l\Delta T_{i0}^{ef}}{L}\right]-\frac{\mathrm{St}\,E}{(E+M_0)}\frac{c_l[\Delta T_{a0}-\Gamma(S_a-S_s)]}{L}\right\}\approx 0. \tag{A2}$$

If $M_0 \ll E$, then we can approximate $E+M_0 \approx E$, and (A2) yields a quadratic equation for M_0 which takes the form

$$AM_0^2+(B-C+\mathrm{St_m}A)\,M_0-\mathrm{St_m}C\approx 0,$$

where

$$A=1-\frac{\mathrm{St}}{E}\frac{c_l\Delta T_{i0}^{ef}}{L},\qquad B=\mathrm{St}\frac{c_l\Gamma(S_a-S_s)}{L},\qquad C=\mathrm{St}\frac{c_l\Delta T_{a0}}{L}.$$

The solution with positive root is

$$M_0\approx\frac{C-B-\mathrm{St_m}A+\sqrt{(C-B-\mathrm{St_m}A)^2+4\mathrm{St_m}AC}}{2A}. \tag{A3}$$

Now, if $\Delta T_{a0} \gg \Gamma(S_{a0}-S_s)$, we can neglect $B \ll C$, and (A3) simplifies to

$$M_0\approx\frac{C}{A}\approx\mathrm{St}\frac{c_l\Delta T_{a0}}{L}\left(1-\frac{\mathrm{St}}{E}\frac{c_l\Delta T_{i0}^{ef}}{L}\right)^{-1}. \tag{A4}$$

If we make the final approximation that $\Delta T_{i0}^{ef} \approx -L/c_p$ is dominated by the latent heat contribution at leading order, then $A \approx 1+\mathrm{St}/E$, and (A3)–(A4) simplify to (34), and (36) as described in the main text.

Acknowledgments

The authors thank the editor and three referees for valuable input. S.J.M. acknowledges support from an Undergraduate Research Bursary from the Institute of Physics and Nuffield Foundation, UK. A.J.W. acknowledges support through the research program of the European Union FP7 award PCIG13-GA-2013-618610 SEA-ICE-CFD. The sources of observational data used in this paper are cited and referred to in the reference list, with all derived quantities summarized in tables in the paper and supporting information. All further numerical information is provided in the tables and figures, and was produced by solving the equations stated in the paper.

References

Baines, P. G. (2005), Mixing regimes for the flow of dense fluid down slopes into stratified environments, *J. Fluid Mech.*, *538*, 245–267.

Bintanja, R., G. J. van Oldenborgh, S. S. Drijfhout, B. Wouters, and C. A. Katsman (2013), Important role for ocean warming and increased ice-shelf melt in Antarctic sea-ice expansion, *Nat. Geosci.*, *6*(5), 376–379.

Bo Pedersen, F. (1980), Dense bottom currents in rotating ocean, *J. Hydraul. Div. Am. Soc. Civ. Eng.*, *106*(8), 1291–1308.

Cowton, T. R., D. A. Slater, A. J. Sole, D. N. Goldberg, and P. W. Nienow (2015), Modeling the impact of glacial runoff on fjord circulation and submarine melt rate using a new subgrid-scale parameterization for glacial plumes, *J. Geophys. Res. Oceans*, *120*, 796–812, doi:10.1002/2014JC010324.

Dallaston, M. C., I. J. Hewitt, and A. J. Wells (2015), Channelization of plumes beneath ice shelves, *J. Fluid Mech.*, *785*, 109–134.

De Rydt, J., P. R. Holland, P. Dutrieux, and A. Jenkins (2014), Geometric and oceanographic controls on melting beneath Pine Island Glacier, *J. Geophys. Res. Oceans*, *119*, 2420–2438, doi:10.1002/2013JC009513.

Dutrieux, P., C. Stewart, A. Jenkins, K. W. Nicholls, H. F. J. Corr, E. Rignot, and K. Steffen (2014), Basal terraces on melting ice shelves, *Geophys. Res. Lett.*, *41*, 5506–5513, doi:10.1002/2014GL060618.

Foldvik, A., and T. Gammelsrød (1988), Notes on southern ocean hydrography, sea-ice and bottom water formation, *Palaeogeogr. Palaeoclimatol. Palaeoecol.*, *67*(1–2), 3–17, doi:10.1016/0031-0182(88)90119-8.

Gade, H. G. (1979), Melting of ice in sea water: A primitive model with application to the Antarctic ice shelf and icebergs, *J. Phys. Oceanogr.*, *9*(1), 189–198, doi:10.1175/1520-0485.

Gladstone, C., and A. W. Woods (2014), Detrainment from a turbulent plume produced by a vertical line source of buoyancy in a confined, ventilated space, *J. Fluid Mech.*, *742*, 35–49.

Gudmundsson, G. H., and A. Jenkins (2015), Sensitivity of Pine Island and Thwaites Glaciers to ocean-induced melt investigated using a new physically-based melt parameterisation, *Geophys. Res. Abstr.*, *17*, EGU2015–6751.

Hogg, C. A. R. (2014), The flow of rivers into lakes: Experiments and models., PhD thesis, Univ. of Cambridge, Cambridge, U. K.

Hogg, C. A. R., S. B. Dalziel, H. E. Huppert, and J. Imberger (2016), Inclined gravity currents filling basins: Peeling detrainment and its implications for transport and vertical structure in basins (sub judice).

Holland, D. M., R. H. Thomas, B. de Young, M. H. Ribergaard, and B. Lyberth (2008a), Acceleration of Jakobshavn Isbrae triggered by warm subsurface ocean waters, *Nat. Geosci.*, *1*(10), 659–664.

Holland, P. R. (2008), A model of tidally dominated ocean processes near ice shelf grounding lines, *J. Geophys. Res.*, *113*, C11002, doi:10.1029/2007JC004576.

Holland, P. R., A. Jenkins, and D. M. Holland (2008b), The response of ice shelf basal melting to variations in ocean temperature, *J. Clim.*, *21*(11), 2558–2572, doi:10.1175/2007JCLI1909.1.

Hughes, G. O., and R. W. Griffiths (2006), A simple convective model of the global overturning circulation, including effects of entrainment into sinking regions, *Ocean Modell.*, *12*, 46–79.

Huppert, H. E., and J. S. Turner (1978), On melting icebergs, *Nature*, *271*(5640), 46–48.

Huppert, H. E., and J. S. Turner (1980), Ice blocks melting into a salinity gradient, *J. Fluid Mech.*, *100*, 367–384, doi:10.1017/S0022112080001206.

IPCC (2013), *Climate Change 2013: The Physical Science Basis. Contribution of Working Group I to the Fifth Assessment Report of the Intergovernmental Panel on Climate Change*, 1535 pp., Cambridge Univ. Press, Cambridge, U. K., doi:10.1017/CBO9781107415324.

Jacobs, S. S., H. E. Huppert, G. Holdsworth, and D. J. Drewry (1981), Thermohaline steps induced by melting of the Erebus Glacier tongue, *J. Geophys. Res.*, *86*(C7), 6547–6555, doi:10.1029/JC086iC07p06547.
Jacobs, S. S., A. Jenkins, C. F. Giulivi, and P. Dutrieux (2011), Stronger ocean circulation and increased melting under Pine Island Glacier ice shelf, *Nat. Geosci.*, *4*(8), 519–523.
Jenkins, A. (1991), A one-dimensional model of ice shelf-ocean interaction, *J. Geophys. Res.*, *96*(C11), 20,671–20,677, doi:10.1029/91JC01842.
Jenkins, A. (1993), *The Melting of Continental Ice in the ocean and its Impact on Surface and Bottom Waters*, vol. 12, pp. 217–235, Springer, Berlin, doi:10.1007/978-3-642-85016-5_14.
Jenkins, A. (2011), Convection-driven melting near the grounding lines of ice shelves and tidewater glaciers, *J. Phys. Oceanogr.*, *41*(12), 2279–2294, doi:10.1175/JPO-D-11-03.1.
Jenkins, A., and A. Bombosch (1995), Modeling the effects of frazil ice crystals on the dynamics and thermodynamics of ice shelf water plumes, *J. Geophys. Res.*, *100*(C4), 6967–6981, doi:10.1029/94JC03227.
Jenkins, A., K. W. Nicholls, and H. F. J. Corr (2010), Observation and parameterization of ablation at the base of Ronne Ice Shelf, Antarctica, *J. Phys. Oceanogr.*, *40*(10), 2298–2312, doi:10.1175/2010JPO4317.1.
Josberger, E. G. (1978), A laboratory and field study of iceberg deterioation, in *Iceberg Utilization: Proceedings of the First International Conference*, edited by A. A. Husseiny, pp. 245–264, Pergamon Press, N. Y.
Kerr, R. C., and C. D. McConnochie (2015), Dissolution of a vertical solid surface by turbulent compositional convection, *J. Fluid Mech.*, *765*, 211–228, doi:10.1017/jfm.2014.722.
Kimura, S., P. R. Holland, A. Jenkins, and M. Piggott (2014), The effect of meltwater plumes on the melting of a vertical glacier face, *J. Phys. Oceanogr.*, *44*(12), 3099–3117, doi:10.1175/JPO-D-13-0219.1.
Kochergin, V. P. (1987), *Three-Dimensional Prognostic Models*, pp. 201–208, AGU, Washington, D. C., doi:10.1029/CO004p0201.
Lane-Serff, G. F. (1995), On meltwater under ice shelves, *J. Geophys. Res.*, *100*(C4), 6961–6965, doi:10.1029/94JC03244.
Lewis, E. L., and R. G. Perkin (1986), Ice pumps and their rates, *J. Geophys. Res.*, *91*(C10), 11,756–11,762, doi:10.1029/JC091iC10p11756.
Little, C. M., A. Gnanadesikan, and M. Oppenheimer (2009), How ice shelf morphology controls basal melting, *J. Geophys. Res.*, *114*, C12007, doi:10.1029/2008JC005197.
Meyer, C. R., and P. F. Linden (2014), Stratified shear flow: Experiments in an inclined duct, *J. Fluid Mech.*, *753*, 242–253.
Morton, B. R., G. Taylor, and J. S. Turner (1956), Turbulent gravitational convection from maintained and instantaneous sources, *Proc. R. Soc. London A*, *234*(1196), 1–23.
Mueller, R. D., L. Padman, M. S. Dinniman, S. Y. Erofeeva, H. A. Fricker, and M. A. King (2012), Impact of tide-topography interactions on basal melting of Larsen C Ice Shelf, Antarctica, *J. Geophys. Res.*, *117*, C05005, doi:10.1029/2011JC007263.
O'Leary, M., and P. Christoffersen (2013), Calving on tidewater glaciers amplified by submarine frontal melting, *Cryosphere*, *7*(1), 119–128, doi:10.5194/tc-7-119-2013.
Payne, A. J., P. Holland, A. P. Shepherd, I. C. Rutt, A. Jenkins, and I. Joughin (2007), Numerical modeling of ocean-ice interactions under Pine Island Bay's ice shelf, *J. Geophys. Res.*, *112*, C10019, doi:10.1029/2006JC003733.
Pollard, D., and R. M. DeConto (2009), Modelling West Antarctic ice sheet growth and collapse through the past five million years, *Nature*, *458*(7236), 329–332.
Pritchard, H. D., S. R. M. Ligtenberg, H. A. Fricker, D. G. Vaughan, M. R. van den Broeke, and L. Padman (2012), Antarctic ice-sheet loss driven by basal melting of ice shelves, *Nature*, *484*(7395), 502–505.
Rignot, E., S. Jacobs, J. Mouginot, and B. Scheuchl (2013), Ice-shelf melting around Antarctica, *Science*, *341*(6143), 266–270, doi:10.1126/science.1235798.
Sciascia, R., F. Straneo, C. Cenedese, and P. Heimbach (2013), Seasonal variability of submarine melt rate and circulation in an East Greenland fjord, *J. Geophys. Res. Oceans*, *118*, 2492–2506, doi:10.1002/jgrc.20142.
Sergienko, O. V., D. N. Goldberg, and C. M. Little (2013), Alternative ice shelf equilibria determined by ocean environment, *J. Geophys. Res. Earth Surf.*, *118*, 970–981, doi:10.1002/jgrf.20054.
Slater, D. A., P. W. Nienow, T. R. Cowton, D. N. Goldberg, and A. J. Sole (2015), Effect of near-terminus subglacial hydrology on tidewater glacier submarine melt rates, *Geophys. Res. Lett.*, *42*, 2861–2868, doi:10.1002/2014GL062494.
Straneo, F., and C. Cenedese (2015), The dynamics of Greenland's glacial fjords and their role in climate, *Annu. Rev. Mar. Sci.*, *7*(1), 89–112, doi:10.1146/annurev-marine-010213-135133.
Straneo, F., R. G. Curry, D. A. Sutherland, G. S. Hamilton, C. Cenedese, K. Vage, and L. A. Stearns (2011), Impact of fjord dynamics and glacial runoff on the circulation near Helheim Glacier, *Nat. Geosci.*, *4*(5), 322–327.
Straneo, F., D. A. Sutherland, D. Holland, C. Gladish, G. S. Hamilton, H. L. Johnson, E. Rignot, Y. Xu, and M. Koppes (2012), Characteristics of ocean waters reaching Greenland's glaciers, *Ann. Glaciol.*, *53*, 202–210, doi:10.3189/2012AoG60A059.
Straneo, F., et al. (2013), Challenges to understanding the dynamic response of Greenland's marine terminating glaciers to oceanic and atmospheric forcing, *Bull. Am. Meteorol. Soc.*, *94*(8), 1131–1144, doi:10.1175/BAMS-D-12-00100.1.
Vellinga, M., and R. A. Wood (2002), Global climatic impacts of a collapse of the Atlantic thermohaline circulation, *Clim. Change*, *54*(3), 251–267, doi:10.1023/A:1016168827653.
Walker, R. T., T. K. Dupont, B. R. Parizek, and R. B. Alley (2008), Effects of basal-melting distribution on the retreat of ice-shelf grounding lines, *Geophys. Res. Lett.*, *35*, L17503, doi:10.1029/2008GL034947.
Wells, A. J. (2008), Natural convection boundary layers and their influence on phase change in the polar oceans, PhD thesis, Univ. of Cambridge, Cambridge, U. K.
Wells, A. J., and M. G. Worster (2008), A geophysical-scale model of vertical natural convection boundary layers, *J. Fluid Mech.*, *609*, 111–137, doi:10.1017/S0022112008002346.
Wells, A. J., and M. G. Worster (2011), Melting and dissolving of a vertical solid surface with laminar compositional convection, *J. Fluid Mech.*, *687*, 118–140.
Wells, M., C. Cenedese, and C. P. Caulfield (2010), The relationship between flux coefficient and entrainment ratio in density currents, *J. Phys. Oceanogr.*, *40*(12), 2713–2727, doi:10.1175/2010JPO4225.1.
Wells, M. G., and J. S. Wettlaufer (2005), Two-dimensional density currents in a confined basin, *Geophys. Astrophys. Fluid Dyn.*, *99*(3), 199–218, doi:10.1080/03091920500094456.
Wells, M. G., and J. S. Wettlaufer (2007), The long-term circulation driven by density currents in a two-layer stratified basin, *J. Fluid Mech.*, *572*, 37–58, doi:10.1017/S0022112006003478.
Woods, A. W. (1992), Melting and dissolving, *J. Fluid Mech.*, *239*, 429–448.

Xu, Y., E. Rignot, D. Menemenlis, and M. Koppes (2012), Numerical experiments on subaqueous melting of Greenland tidewater glaciers in response to ocean warming and enhanced subglacial discharge, *Ann. Glaciol.*, *53*, 229–234, doi:10.3189/2012AoG60A139.

Xu, Y., E. Rignot, I. Fenty, D. Menemenlis, and M. M. Flexas (2013), Subaqueous melting of Store Glacier, west Greenland from three-dimensional, high-resolution numerical modeling and ocean observations, *Geophys. Res. Lett.*, *40*, 4648–4653, doi:10.1002/grl.50825.